Interaction between a Vertical Turbulent Jet and a Thermocline

EKATERINA EZHOVA

Linné FLOW Centre, and Swedish e-Science Research Centre, KTH Mechanics, Stockholm, Sweden

CLAUDIA CENEDESE

Physical Oceanography Department, Woods Hole Oceanographic Institution, Woods Hole, Massachusetts

LUCA BRANDT

Linné FLOW Centre, and Swedish e-Science Research Centre, KTH Mechanics, Stockholm, Sweden

(Manuscript received 31 January 2016, in final form 30 August 2016)

ABSTRACT

The behavior of an axisymmetric vertical turbulent jet in an unconfined stratified environment is studied by means of well-resolved, large-eddy simulations. The stratification is two uniform layers separated by a thermocline. This study considers two cases: when the thermocline thickness is small and on the order of the jet diameter at the thermocline entrance. The Froude number of the jet at the thermocline varies from 0.6 to 1.9, corresponding to the class of weak fountains. The mean jet penetration, stratified turbulent entrainment, jet oscillations, and the generation of internal waves are examined. The mean jet penetration is predicted well by a simple model based on the conservation of the source energy in the thermocline. The entrainment coefficient for the thin thermocline is consistent with the theoretical model for a two-layer stratification with a sharp interface, while for the thick thermocline entrainment is larger at low Froude numbers. The data reveal the presence of a secondary horizontal flow in the upper part of the thick thermocline, resulting in the entrainment of fluid from the thermocline rather than from the upper stratification layer. The spectra of the jet oscillations in the thermocline display two peaks, at the same frequencies for both stratifications at fixed Froude number. For the thick thermocline, internal waves are generated only at the lower frequency, since the higher peak exceeds the maximal buoyancy frequency. For the thin thermocline, conversely, the spectra of the internal waves show the two peaks at low Froude numbers, whereas only one peak at the lower frequency is observed at higher Froude numbers.

1. Introduction

This study focuses on the dynamics of an axisymmetric vertical turbulent jet in a stratified fluid. Vertical turbulent jets may serve as models of numerous flows both in nature and industry (see, e.g., Turner 1973; List 1982; Hunt 1994), including effluents from submerged wastewater outfall systems in the ocean (e.g., Jirka and Lee 1994), convective cloud flows in the atmosphere, pollutant discharge from industrial chimneys, and subglacial discharge from glaciers (e.g., Straneo and Cenedese 2015). The stratification considered is two layers of homogeneous fluids of different temperature separated by a relatively thin layer with a temperature jump—a thermocline. This configuration is a typical model of the upper thermocline layer in lakes, the pycnocline in the ocean, as well as thermal inversions in the atmosphere, when the sharp gradient of the scalar prevails significantly over the scalar change in the layers.

The dynamics of vertical jets is governed mainly by their volume, momentum, and buoyancy fluxes, where the buoyancy of a jet is defined by the density difference between the jet and the surrounding medium, normalized by gravity. If the flow density is less than the density of the surrounding medium then the jet is positively buoyant; if it is heavier, the jet is negatively buoyant, while it is neutrally buoyant if the densities are equal. In general, all the examples of turbulent jets in nature and industry mentioned above result from mixed sources of

Corresponding author address: Ekaterina Ezhova, Linné FLOW Centre and Swedish e-Science Research Centre, KTH Mechanics, Osquars Backe 18, 10044 Stockholm, Sweden.
E-mail: eezhova@mech.kth.se

DOI: 10.1175/JPO-D-16-0035.1

buoyancy and momentum (as a rule they are positively buoyant). However, jets effectively entrain the surrounding fluid; hence, when the source is located far enough from the pycnocline, the density of the flow at the pycnocline entrance is almost equal to the density of the lower layer of stratification. The dynamics of such a flow in the pycnocline can therefore be modeled employing a neutrally buoyant turbulent jet with positive vertical momentum in the lower stratification layer. In other words, an initially buoyant jet in the pycnocline can be modeled employing a neutrally buoyant jet, provided they have the same velocity and radius at the entrance of the pycnocline. The turbulent jet considered here results from a momentum source of the same fluid as in the lower layer of stratification. When entering the thermocline, it becomes a negatively buoyant jet, that is, a fountain.

Stationary regimes of turbulent fountains have been extensively investigated in both homogeneous and linearly stratified media (Turner 1966; List 1982; Bloomfield and Kerr 1998, 2000; Kaye and Hunt 2006; Burridge and Hunt 2012, 2013), revealing the dependency of the mean penetration height and of the entrainment coefficient on the different parameters of the problem. The behavior of an axisymmetric, miscible, Boussinesq fountain in a homogeneous fluid is defined by the Reynolds number $\mathrm{Re} = U_0 R_0/\nu$ (U_0 is the inflow velocity, R_0 is the nozzle radius, and ν is the fluid kinematic viscosity) and the Froude number $\mathrm{Fr} = U_0/\sqrt{g' R_0}$ (with $g' = g\Delta\rho/\rho_0$, the reduced gravity, and $\Delta\rho$ is the density difference between source and ambient fluid). The Reynolds number determines whether the fountain is laminar or turbulent, while the Froude number characterizes the ratio between momentum flux M_0, buoyancy flux F_0, and volume flux Q_0 of the fountain. Indeed, it can be rewritten, following Kaye and Hunt (2006), as $\mathrm{Fr} \sim M_0^{5/4}/Q_0 F_0^{1/2}$. The Froude number can also be interpreted as the ratio between two length scales: $l \sim M_0^{3/4}/F_0^{1/2}$, known as the momentum jet length (Turner 1966), and $R_0 \sim Q_0/M_0^{1/2}$, corresponding to the initial radius of the jet. Using theoretical considerations and experimental validations, Kaye and Hunt (2006) classified fountains according to their Froude number as very weak ($\mathrm{Fr} \lesssim 1$), weak ($1 \lesssim \mathrm{Fr} \lesssim 3$), and forced ($\mathrm{Fr} \gtrsim 3$). Later Burridge and Hunt (2012, 2013) extended the classification using more experimental data, further dividing "weak fountains" into weak and intermediate, with a change from weak to intermediate fountains at $\mathrm{Fr} \approx 1.7$. The behavior of forced fountains in a homogeneous fluid is governed by the momentum and buoyancy fluxes, and the mean penetration height, here denoted h_z, is therefore proportional to the momentum jet length $h_z/R_0 \sim \mathrm{Fr}$ (Turner 1966). For weak fountains, instead, all three fluxes are important, and dimensional analysis gives a penetration $h_z/R_0 \sim \mathrm{Fr}^2$ (Kaye and Hunt 2006; Burridge and Hunt 2012). Finally, very weak fountains are hydraulically controlled, and estimates at large Reynolds numbers give $h_z/R_0 \sim \mathrm{Fr}^{2/3}$ (Kaye and Hunt 2006; Burridge and Hunt 2012).

In a linear stratification, dimensional considerations yield a penetration height $h_z/R_0 \sim \mathrm{Fr}^{1/2}$ for forced fountains with zero initial buoyancy flux (McDougall 1981; Bloomfield and Kerr 1998). In general, however, the rise height of a fountain in a stratified fluid depends on the density profile and requires more complicated numerical models based on the conservation laws for the momentum, volume, and buoyancy fluxes of the jet (Morton et al. 1956; Bloomfield and Kerr 2000).

Instabilities are observed for fountains in a homogeneous fluid, and this oscillatory motion has become the object of research only recently (Friedman 2006; Friedman et al. 2007; Williamson et al. 2008; Burridge and Hunt 2013). The dynamics of a fountain in a homogeneous fluid is, analogously to the mean penetration height, fully controlled by the Froude and Reynolds numbers. It has been demonstrated experimentally that weak fountains can undergo oscillations with amplitudes comparable to their heights and well-defined frequencies. The oscillatory dynamics of fountains in stratified fluids is, however, mostly unexplored. Interestingly, the only experimental investigation in a linear stratification has shown no direct connection between the frequency of the fountain oscillations and the frequency of internal waves (Ansong and Sutherland 2010).

A behavior similar to the oscillatory dynamics of weak fountains has been revealed in pycnocline-like stratified fluids while modeling submerged wastewater outfall systems in the ocean (Troitskaya et al. 2008). Turbulent buoyant plumes discharged horizontally into oceanic saltwater gain vertical momentum due to their positive buoyancy while they propagate in the lower layer of stratification. At the same time, they are mixing intensively with the surrounding fluid owing to the turbulent entrainment. At the entrance to the pycnocline, these jets have density close to the density of the lower layer of stratification and a nonzero vertical momentum, thus forming fountains. These fountains are capable of generating internal waves in a pycnocline through their oscillations. This effect has been demonstrated experimentally, by means of laboratory-scale modeling of wastewater outfall systems, and later numerically (Druzhinin and Troitskaya 2012, 2013) both for laminar and turbulent fountains/jets in two-layer, stratified fluid with a thin pycnocline (i.e., in the presence of a rather sharp density jump compared to the jet diameter at the pycnocline entrance).

As mentioned earlier, fountains in a linear stratified fluid do not show pronounced oscillations, while fountains in a two-layer fluid are characterized by strong oscillations. Thus, in addition to the Reynolds and Froude number, with all these parameters taken in the vicinity of the pycnocline, the ratio of the pycnocline thickness to the jet diameter is expected to play an important role. Therefore, the aim of this paper is to understand the influence of the ratio ''pycnocline thickness/jet diameter'' on the dynamics of a turbulent fountain and on the generation of internal waves, using data from well-resolved, large-eddy simulation (LES). Since the pycnocline is subject to seasonal variability (Kamenkovich and Monin 1978; Knauss 2005; Stewart 2008), this ratio is expected to change throughout the year, making this a relevant question in oceanography.

Previous numerical investigations (Druzhinin and Troitskaya 2012, 2013) investigated a similar configuration but focused on a thin pycnocline in comparison to the jet diameter at the pycnocline entrance. However, field measurements and results of modeling employing nonhydrostatic general circulation models reveal that they are mostly of the same size (Sciascia et al. 2013; Troitskaya et al. 2008). In this paper, we compare jet dynamics in two different stratifications: one with a thin thermocline, analogous to Druzhinin and Troitskaya (2013), and the other with a thermocline thickness close to the jet diameter at the thermocline entrance. The latter case, for the thermocline Froude numbers 0.87–1.16, reproduces the conditions of laboratory experiments investigating the generation of internal waves by a turbulent jet (Ezhova et al. 2012). Note that the parameters of the jet at the entrance to the thermocline in the experiments matched the parameters of the laboratory-scale modeling of the real wastewater outfall system in winter conditions (Troitskaya et al. 2008). In summer, convection in the upper layer is weak, governed mainly by the surface wave breaking and mixing due to the wind; together with the increased temperature difference between upper and lower layers this results in the sharpening of the pycnocline and its moving closer to the surface. As a result, for the same source location, the radius of the jet at the pycnocline entrance increases and the vertical velocity decreases; some qualitative conclusions about the jet dynamics in these conditions can therefore be drawn from the present results for the thin thermocline and low Froude numbers.

The jet dynamics in the thermocline is relevant for turbulent mixing of the jet with the surrounding media. This important question has been before investigated for a jet in two-layer stratification with a density interface experimentally (Cotel et al. 1997; Lin and Linden 2005) and theoretically (Shrinivas and Hunt 2014, 2015). In this study, we investigate the mean flows in the thermocline and compare the entrainment flux of the jet in stratifications characterized by a finite thickness of the thermocline with the results of the theoretical model by Shrinivas and Hunt (2014).

The paper is organized as follows: Section 2 contains the relevant equations and a brief description of the LES model. The test case of a turbulent jet in a homogeneous medium is described, and the setup of the simulations for a stratified case is discussed. Section 3 is devoted to the results of the simulations: in the first part, we investigate the penetration height and turbulent entrainment of the jet in a stratified medium and discuss the dynamics of the jet in the thermocline. The generation of the internal waves is presented in the second part. Our conclusions are given in section 4.

2. Governing equations and numerical method

We consider a jet in an unconfined fluid with a stable thermal stratification. The dynamics of a jet in a stratified fluid is governed by the Navier–Stokes equations for an incompressible fluid with the Boussinesq approximation to model the buoyancy effects and a transport equation for the temperature field. To carry out a parameter study like that presented here, we resort to LES to reduce the computational costs. In a LES, the large turbulent eddies are fully resolved, whereas the effect of the smallest scales, those not resolved on the computational mesh, is modeled. A filter is applied to derive an equation for the resolved scales that reads in dimensionless form and in a Cartesian coordinate system:

$$\frac{\partial u_i}{\partial t} + u_j \frac{\partial u_i}{\partial x_j} = -\frac{\partial p}{\partial x_i} + \frac{1}{\mathrm{Re}} \frac{\partial^2 u_i}{\partial x_j^2} + \frac{1}{\mathrm{Fr}^2}(T - T_s')\delta_{iz} - \frac{1}{\mathrm{Re}} \frac{\partial \tau_{ij}}{\partial x_j}, \tag{1}$$

$$\frac{\partial T}{\partial t} + u_j \frac{\partial T}{\partial x_j} = \frac{1}{\mathrm{RePr}} \frac{\partial^2 T}{\partial x_j^2} - \frac{1}{\mathrm{Re}} \frac{\partial \Theta_j}{\partial x_j}, \quad \text{and} \tag{2}$$

$$\frac{\partial u_i}{\partial x_i} = 0. \tag{3}$$

The equations are made dimensionless with the initial jet diameter D_0, the jet maximal inflow velocity U_0, and the temperature difference between the stratification layers ΔT. Nondimensional coordinates x_i stand for x, y, and z, and nondimensional velocity components u_i stand for u_x, u_y, and u_z. We define the profile of stratification as $T_s' = (T_s - T_0)/\Delta T$, where T_s is the undisturbed temperature profile, and T_0 is the temperature of the lower layer of stratification. The hydrostatic pressure component associated with T_s' is subtracted from the full pressure to get p in our system. We define the Reynolds

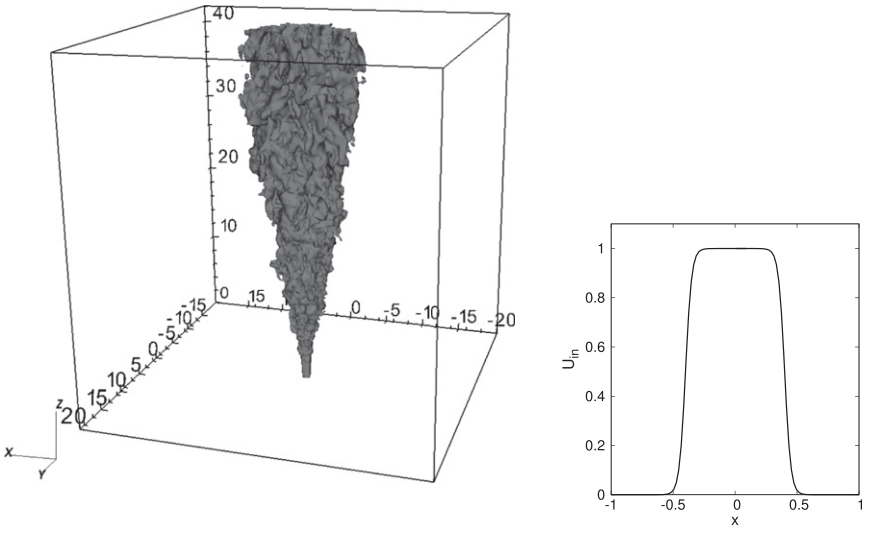

FIG. 1. (left) Domain configuration for the turbulent jet in a homogeneous fluid. The jet is shown by the contour surface of vertical velocity $u_z = 0.03$. (right) An inflow velocity profile.

number $\mathrm{Re} = U_0 D_0/\nu$; the Froude number $\mathrm{Fr} = U_0/\sqrt{g' D_0}$, with $g' = g\Delta\rho/\rho_0 \approx g a_T \Delta T$ as the reduced gravity (here a_T is the thermal expansion coefficient); and the Prandtl number $\mathrm{Pr} = \nu/\kappa$, where ν is the fluid kinematic viscosity and κ is the thermal conductivity. The terms τ_{ij} and Θ_j are the fluxes representing the subgrid Reynolds stresses and turbulent heat transport.

To model the subgrid-scale stresses, we employ the dynamic Smagorinsky model (Smagorinsky 1963; Germano et al. 1991) that has been successfully used in the simulations of buoyant flows by several authors (e.g., Pham et al. 2006, 2007). The subgrid-scale stresses are expressed as

$$\tau_{ij} = -2\nu_t S_{ij}, S_{ij} = \frac{1}{2}\left(\frac{\partial u_i}{\partial x_j} + \frac{\partial u_j}{\partial x_i}\right), \quad \text{and} \tag{4}$$

$$\Theta_j = -\frac{\nu_t}{\mathrm{Pr}_t}\frac{\partial T}{\partial x_j}. \tag{5}$$

In the spirit of the Prandtl mixing length model, the subgrid-scale viscosity is given by the formula

$$\nu_t = (C_s\Delta)^2 |S_{ij}|, \tag{6}$$

where $\Delta = (\Delta x \Delta y \Delta z)^{1/3}$ and C_s is the Smagorinsky coefficient, related to the dynamic Smagorinsky constant by $C_s = \sqrt{C_d}$. The idea underlying the dynamic Smagorinsky model is that the small eddies of the large structures that are still resolved in the computations are statistically analogous to the subgrid-scale eddies. Thus, an additional filter, the test filter, is used to separate the resolved turbulent spectrum and calculate dynamically the Smagorinsky constant C_d [for more detail see Germano et al. (1991)].

In our simulations, the jet is generated by a round source of diameter D_0 with an initial vertical velocity profile

$$U_i = -0.5 \tanh\frac{r - 0.4}{0.05} + 0.5, \tag{7}$$

where $r = \sqrt{x^2 + y^2}$, with x and y the horizontal directions (see Fig. 1). The stratification of the ambient fluid is of a thermocline type with a temperature jump at the vertical position $z = z_p$. The stratification profile is given by

$$T_s' = \frac{1}{2}\{1 + \tanh[\gamma(z - z_p)]\}, \tag{8}$$

where $\gamma = D_0/H$, and H is the half-thickness of the thermocline. The temperature of the fluid at the inflow is equal to the temperature of the lower stratification layer.

a. Numerical method

The numerical simulations presented here are performed with the parallel flow solver Nek5000 (Fischer et al. 2008). The dynamic Smagorinsky model is built-in inside this code. Nek5000 is a spectral element code with exponential accuracy within the spectral elements. On each element the flow variables are represented as a superposition of Lagrange polynomials based on Gauss–Lobatto–Legendre quadrature points (GLL points). In the present calculations, the spatial discretization is made with polynomials of order seven, which means that each element contains $8 \times 8 \times 8$ grid points or GLL points. Time discretization involves an operator-splitting

method using backward differentiation of order two for the implicitly treated viscous terms and second-order extrapolation for the explicitly treated convective terms (BDF2/EXT2). For stabilization, the highest two modes of each element are slightly dampened (5%). The test filter required for the calculations in the framework of the dynamic Smagorinsky model affects the three highest polynomial modes with a cutoff of 0.05, 0.5, and 0.95 (Ohlsson et al. 2010).

Among the advantages of the spectral element method is the flexibility to construct spatially inhomogeneous meshes. For the particular problem at hand, one needs to resolve the small scales at the jet inflow to accurately reproduce the region of high kinetic energy production and the small scales in the region where the jet impinges on the pycnocline, producing high shears. At the same time, internal gravity waves are characterized by long wavelengths and large-scale motions, so that a lower resolution is enough at larger distances from the jet axis.

b. *Validation for the turbulent jet in a nonstratified fluid*

To validate the current implementation and be sure to have a fully developed turbulent jet at the thermocline entrance, we perform LES of a turbulent jet in a homogeneous fluid and compare the main flow statistics with the data available in literature, both from experiments and direct numerical simulations (DNS).

The governing equations for a turbulent jet in a homogeneous fluid reduce, after the LES filtering, to

$$\frac{\partial u_i}{\partial t} + u_j \frac{\partial u_i}{\partial x_j} = -\frac{\partial p}{\partial x_i} + \frac{1}{\mathrm{Re}} \frac{\partial^2 u_i}{\partial x_j^2} - \frac{1}{\mathrm{Re}} \frac{\partial \tau_{ij}}{\partial x_j}, \quad \text{and} \tag{9}$$

$$\frac{\partial u_i}{\partial x_i} = 0. \tag{10}$$

The jet is generated at the bottom boundary of the computational domain and has a round shape of diameter D_0 with the initial velocity profile given in Eq. (7). To trigger transition to turbulence, we add to this laminar profile a set of 10 sinusoidal disturbances with frequencies f distributed evenly in the range [0.05: 5], wavelengths in x, y directions changing from four minimal distances between GLL points ($\Delta x = \Delta y = 0.03$) to 20 times these distances, and random phases. The amplitude of the disturbances is about 15% of the base flow velocity at the inflow. The simulations are performed for Reynolds number $\mathrm{Re} = 15\,000$.

We solve the governing equations on a rectangular domain of dimensions 40×40 along the horizontal x and y axes and 42 in the vertical direction (Fig. 1). We impose a traction-free boundary condition (open boundaries) at the lateral boundaries and the convective boundary condition by Orlanski (1976),

$$\frac{\partial u_i}{\partial t} + c_{zi} \frac{\partial u_i}{\partial z} = 0, \tag{11}$$

at the top of the domain. Here, c_{zi} are the components of the phase velocity that are calculated dynamically for each velocity component at the z level adjacent to the upper boundary and filtered over the x–y plane by a running average. Negative values of c_{zi} are set to 0.

The mesh used is constructed following the guidelines in Picano and Hanjalic (2012): in the region closest to the jet inflow, $x, y \in [-1.5, 1.5]$ and $z \in [0, 12]$, a better resolution is achieved with uniform spectral elements of size $\Delta x = \Delta y = 0.5$ and $\Delta z = 0.6$ (each element containing $8 \times 8 \times 8$ GLL points). From the boundaries of this inner region, we stretch the grid by a factor 1.17 along the horizontal axes and 1.06 along the z axis. The total number of elements used in these validation runs is $30 \times 30 \times 30$ corresponding to ≈9 million grid points. The time step chosen for the calculation is 0.01, which amounts to keeping the CFL number below 0.25–0.3.

The values of C_d in the model are averaged over the vertical direction in a conical region containing the jet, resulting in a value of the Smagorinsky coefficient C_s in the range between 0 and 0.2, in agreement, for example, with the values obtained in the simulations of buoyant plumes by Pham et al. (2007). The calculations of the statistics start approximately 100 time units after the jet has reached the upper boundary and extend over a time interval of over 500 dimensionless time units corresponding to ≈30 eddy turnover times if the characteristic velocity and the jet diameter are taken at $z = 18$.

Figure 2a displays the inverse, centerline, mean velocity U_c versus the vertical coordinate z to show that the velocity follows the $1/z$ dependence that can be derived from the momentum integral for a submerged turbulent jet. The asymptotic behavior starts from $z \approx 12$. The linear fit yields a slope of 0.22, corresponding to 0.165 if recalculated for the initial top-hat velocity profile with the same momentum and volume fluxes. This is in good agreement with the widely assumed values of 0.16–0.17 [see, for instance, Pope (2000)].

Figure 2b displays the average z-velocity profile in the far field of the jet in self-similar coordinates [$\xi \sim r/(z - z_0)$, U/U_c], where z_0 denotes the location of the jet virtual origin and U_c corresponds to the maximum velocity at each z level. In practice, we first compute the profiles at each z in self-similar variables and then average over the different profiles in the range $z \in [14, 35]$, following Picano and Hanjalic (2012), among others. In the figure, we include for comparison the data from two sets

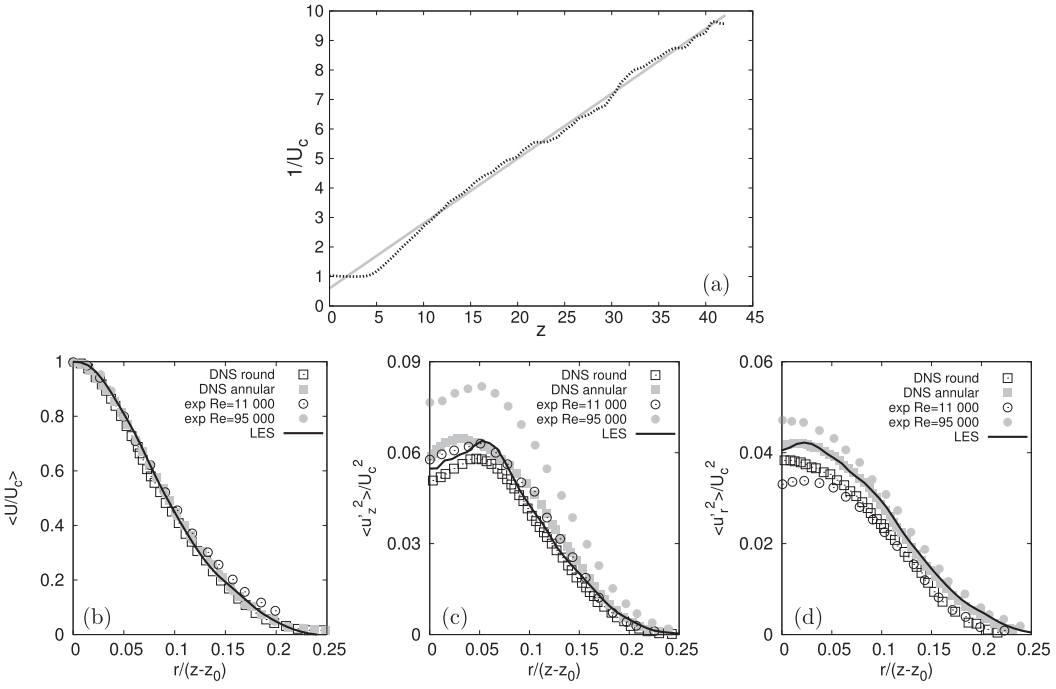

FIG. 2. (a) Inverse mean centerline velocity as a function of the distance from the nozzle (black dots indicate LES data, gray indicates theory). (b) The far-field z-velocity profile, (c) turbulent stresses $\langle u_z'^2\rangle/U_c^2$, and (d) $\langle u_r'^2\rangle/U_c^2$. The data for comparison are available from the following papers: DNS round can be found in Picano and Casciola (2007), DNS annular can be found in Picano and Hanjalic (2012), exp Re = 11 000 can be found in Panchapakesan and Lumley (1993), and exp Re = 95 000 can be found in Hussein et al. (1994).

of DNS for the round and annular jets (Picano and Hanjalic 2012; Picano and Casciola 2007) and two laboratory experiments (Panchapakesan and Lumley 1993; Hussein et al. 1994) to confirm the accuracy of the results.

Figures 2c and 2d report the turbulent stresses $\langle u_z'^2\rangle/U_c^2$ and $\langle u_r'^2\rangle/U_c^2$ in the far field of the turbulent jet together with the data from the experiments and DNS mentioned above. To obtain $\langle u_r'^2\rangle$ in the rectangular geometry, we measure the profiles of $\langle u_x'^2\rangle$ along the x axis and of $\langle u_y'^2\rangle$ along the y axis and then average over the positive and negative x and y directions. We scale the profiles using the self-similar coordinates and average among the different z locations as described before. It can be seen in the figure that the agreement between the different sets of data is good. Given these data, we consider a developed turbulent jet from $z = 14$ and therefore set, in the calculations in a stratified medium, the thermocline lower boundary at $z = 20$.

c. *Configuration of the jet in a stratified fluid*

Using the governing equations for a flow in a stratified medium in Eqs. (1)–(3), we perform two series of simulations with the stratification profile in Eq. (8). The first set assumes $\gamma = 2$ and $z_p = 20.5$, which corresponds to a relatively thin thermocline since the jet diameter at the entrance to the thermocline is approximately 4–5, as shown by the simulation of a turbulent jet in homogeneous medium presented in the previous section. Indeed, for $\gamma = 2$ the thermocline is 4–5 times thinner than the diameter of the jet. The second set of simulations assume $\gamma = 0.5$ and $z_p = 22$, which we will denote as the thick thermocline; in this case, the thermocline thickness is approximately the same as the jet diameter at the thermocline entrance. In both series we perform calculations for five different Froude numbers (Fr = 7, 10, 13, 16, and 22).

Better definitions of the Froude number and γ may consider values at the entrance to the thermocline, which is defined from the simulations at approximately $z = 18$ (as it will be seen from what follows), corresponding to $\mathrm{Fr}_t = 0.6$, 0.86, 1.11, 1.37, and 1.89 {here $\mathrm{Fr}_t = u_t/\sqrt{g'R_t}$, where u_t and R_t are the mean jet velocity and radius [Shrinivas and Hunt (2014)], $u_t = 0.5U_{\max}$ with the corresponding R_t at this level}. We define the ratio of the jet radius at the thermocline to the thermocline thickness, $\gamma_t = R_t/H$. For the thick thermocline $\gamma_t \cong 1$, while for the thin thermocline $\gamma_t \cong 4$.

The choice of $\mathrm{Fr}_t \sim 1$ is justified by the observations by Burridge and Hunt (2013) of the sudden jump in the amplitude and frequency of the fountain top oscillations

TABLE 1. Parameters of the simulations of a jet impinging on a thin or thick thermocline. The nominal Froude number is $\mathrm{Fr} = U_0/\sqrt{g'D_0}$, while the thermocline Froude number $\mathrm{Fr}_t = u_t/\sqrt{g'R_t}$ uses the jet mean radius and velocity at $z = 18$ [for comparison with Shrinivas and Hunt (2014, 2015)]; $\gamma = D_0/H$ indicates the inverse thickness of the thermocline.

Fr (Fr_t)	γ	Domain size	No. of spectral elements	No. of grid points
7 (0.60)	2	$80 \times 80 \times 31$	$38 \times 38 \times 36$	26 615 808
10 (0.86)	2	$80 \times 80 \times 31$	$38 \times 38 \times 36$	26 615 808
13 (1.11)	2	$80 \times 80 \times 32$	$38 \times 38 \times 38$	28 094 464
Test 13 (1.37)	2	$80 \times 80 \times 32$	$48 \times 48 \times 45$	53 084 160
16 (1.37)	2	$80 \times 80 \times 33$	$38 \times 38 \times 42$	31 051 776
22 (1.89)	2	$95 \times 95 \times 37$	$40 \times 40 \times 52$	42 598 400
7 (0.60)	0.5	$95 \times 95 \times 32.5$	$40 \times 40 \times 33$	27 033 600
10 (0.86)	0.5	$95 \times 95 \times 33.5$	$40 \times 40 \times 35$	28 672 000
13 (1.11)	0.5	$95 \times 95 \times 34.5$	$40 \times 40 \times 36$	29 491 200
16 (1.37)	0.5	$95 \times 95 \times 35.5$	$40 \times 40 \times 37$	30 310 400
22 (1.89)	0.5	$95 \times 95 \times 40.5$	$40 \times 40 \times 45$	36 364 000

in a homogeneous fluid. Note, however, that the Reynolds number in the experiments of Burridge and Hunt (2013), Re $\approx$ 1000–3500, is significantly lower than in our simulations. The experimental investigation of turbulent jets in a stratified fluid by Ezhova et al. (2012) corresponds to $\mathrm{Fr}_t \sim 1$ and Re $\sim$ 10 000. Given that the diameter of the jet in the experiments was comparable to the thermocline width, we in fact reproduce these experimental conditions in the setup with the thick thermocline.

The coefficient of the dynamic Smagorinsky model C_d is averaged over the vertical direction from $z = 0$ to the maximum fountain penetration point for $r < 5$ and from $z = 17$ to the upper boundary of the thermocline for $r > 5$, resulting in the same range of the Smagorinsky coefficient $0 < C_s = \sqrt{C_d} < 0.2$ as for the test case with a jet in homogeneous fluid (section 2b). We use open boundary conditions on all the boundaries except the inflow where we impose the velocity profile of Eq. (7). On the lateral boundary, we also use a sponge layer to damp the vertical velocity component and the temperature fluctuations. The length of the sponge layer is 5 in the simulations with the thin thermocline and 7 in the simulations with the thick thermocline.

The mesh used for the stratified case has the same stretching as in the test case of a jet in homogeneous fluid in the x and y directions, though in a wider domain to be able to capture the internal waves propagating in the thermocline. However, we refine the mesh and increase the vertical resolution at the thermocline and in the upper layer of the stratification approximately up to the penetration height of the fountain to maintain a well-resolved LES. The parameters pertaining to all simulations are summarized in Table 1, where we also report the case used for the validation with increased resolution discussed in the appendix (denoted as test). The resulting flow is displayed in Fig. 3 for the thick thermocline at Fr = 22.

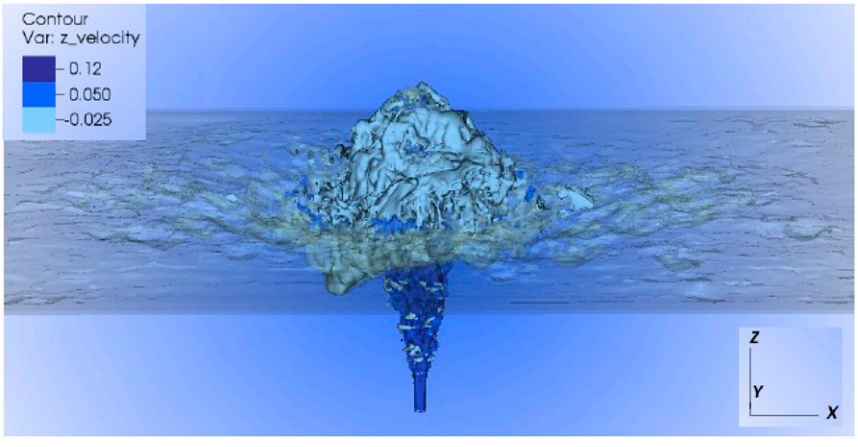

FIG. 3. Illustration of the jet in a stratified fluid by surfaces of constant vertical velocity and temperature for the thick thermocline Fr = 22 (Fr_t = 1.89). Waves are visualized by surfaces of constant temperature T = 0.03 and 0.97.

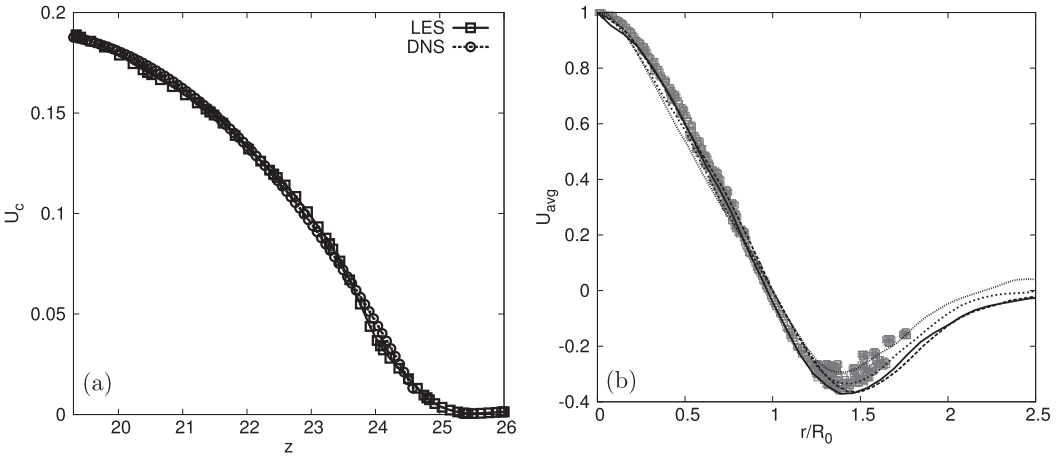

FIG. 4. Comparison of present LES data with DNS and experiments. (a) Mean axial vertical velocity vs z against the DNS data for weak fountains by Lin and Armfield (2000). (b) Mean vertical velocity profiles in the cross sections along the jet axis in the thermocline (curves) against the experimental data on turbulent jets in a stratified fluid by Ezhova and Troitskaya (2012) (symbols).

Validation of our LES model (Fr = 13, thick thermocline) against the data on weak fountains in a homogeneous fluid by Lin and Armfield (2000) and experiments on turbulent jets in a stratified fluid by Ezhova and Troitskaya (2012) is shown in Fig. 4. Figure 4a shows the decay of the axial vertical velocity of the jet in the thermocline versus that of the weak fountain in a homogeneous fluid (Lin and Armfield 2000). Figure 4b shows several LES profiles of the vertical velocity in the thermocline (each normalized by its centerline value U_c, while R_0 corresponds to the distance, where $U_{\text{avg}} = 0$) and compares them to the experimental data by Ezhova and Troitskaya (2012). We do not include DNS data for the fountains in this figure since Lin and Armfield (2000) used an initial parabolic vertical velocity, and the vertical velocity profiles tend to keep the parabolic form in weak fountains; as shown in the figure, the experimental and LES profiles are closer to Gaussian. Thus, the LES model presented here captures the properties of the mean velocity fields of the weak fountains.

For each simulation, we gather statistics (the mean values and the rms of the fluctuations of all quantities) and save time histories to analyze the jet oscillations and the main features of the internal waves at specific locations in the flow. We collect statistics approximately 100 time units after the perturbations at the thermocline have reached the lateral boundary of the computational domain. This time changes from approximately 900 time units for the thin thermocline and small Froude number to about 2100 time units for the thick pycnocline and large Froude number. The duration of the sampling changes from 1200 time units to 4100 time units, with intervals of 0.25 time units for the time histories. To investigate the dynamics of the fountain at the thermocline and the internal waves, we examine the oscillations of the isotherm $T = 0.5$. The jet oscillations are characterized by the isotherms at the center of the jet and at four points at distance $r = 1.5$ from the jet axis, while internal waves are studied by the isotherms corresponding to two sets of points located farther away, at $r = 20$ and 25.

3. Results

We shall first examine the statistics of the flow and, in the following section, consider the internal waves generated by the interaction between the jet and the thermocline.

a. Jet impingement and entrainment

Figure 5 shows cross sections of the absolute value of the mean velocity from our simulations. The first observation is that the higher the Froude number, the higher the jets penetrate into the thermocline and eventually into the upper layer of stratification. For the lowest Fr and the strongest stratification (thin thermocline), the mean flow is reminiscent of a jet impinging on a wall. In the other cases, the flow has a more complicated structure and a counterflow appears in the thermocline and upper stratification layer to form a fountain. This counterflow is more evident when increasing the Froude number and decreasing the thickness of the thermocline. The higher the jet penetrates, the higher the counterflow velocity is and the deeper the annular flow surrounding the jet propagates into the lower layer. Mixing, in turn, makes the fluid in the counterflow lighter than the lower layer of stratification,

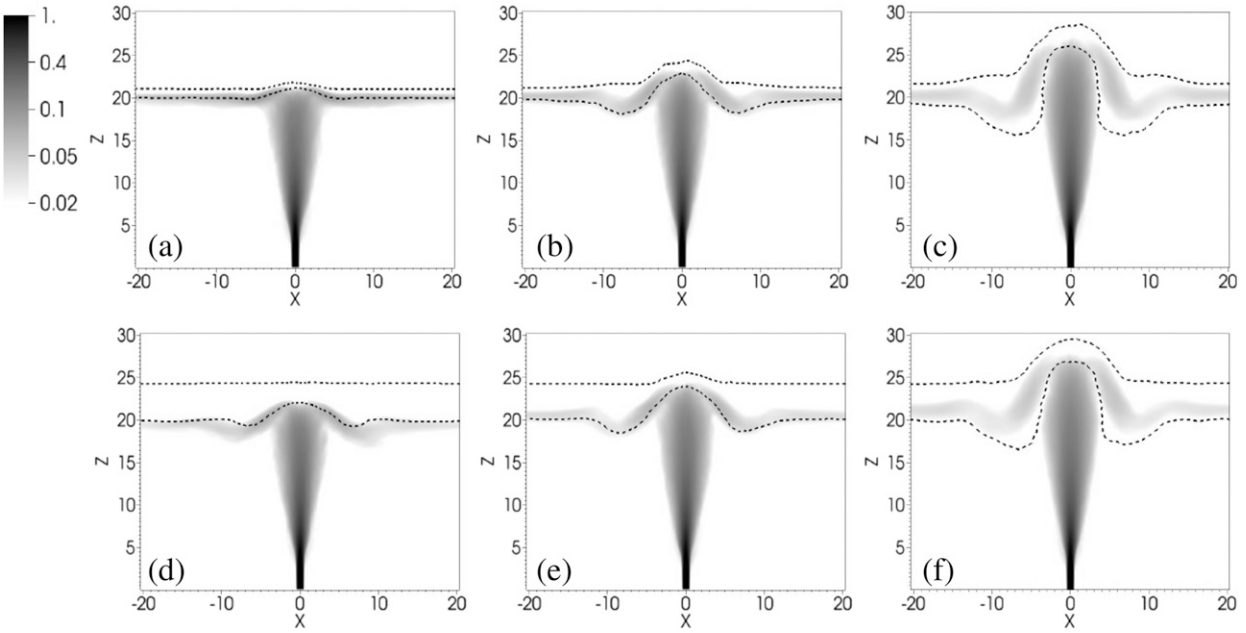

FIG. 5. Magnitude of the mean flow velocity for Fr = (a),(d) 7 (Fr_t = 0.6), (b),(e) 13 (1.11), and (c),(f) 22 (1.89) [(top) thin thermocline and (bottom) thick thermocline]. Dashed curves correspond to the contour lines of temperature T = 0.1 and 0.9.

so that it bounces back to the thermocline where it finally spreads at the level of neutral buoyancy. This structure is characteristic of a two-layer stratification (Cotel et al. 1997; Ansong et al. 2005) as compared to fountains in homogeneous and linearly stratified media, where the counterflow simply protrudes to the bed or to the level of neutral buoyancy (Bloomfield and Kerr 1998).

To quantify the jet penetration into the thermocline, we report the mean axial jet velocity for all the stratified cases and for the turbulent jet in homogeneous medium in Fig. 6a. The evolution in the stratified media follows that in a homogeneous medium to $z \approx 18$, before the typical behavior of a fountain is observed.

Figure 6b reports the penetration heights from the LES defined as the location where the jet velocity falls below 1% of the initial velocity.

The Froude numbers calculated at the thermocline entrance are characteristic of weak fountains, and the rising height can be estimated from the conservation of energy (Kaye and Hunt 2006) so that the source kinetic energy of the flow is converted into potential energy. This implies that

$$\frac{U_m^2}{2} \sim \int_{18D_0}^{h_z^*} g a_T (T_s - T_0)\, dz^*, \tag{12}$$

where U_m is the centerline jet velocity at the level where the fountain is formed (we take $z^* = 18D_0$), and h_z^* is the penetration height. Normalizing Eq. (12) with D_0, U_0, and ΔT, we finally obtain

$$(\lambda u_m)^2 \frac{\mathrm{Fr}^2}{2} = \int_{18}^{h_z} T_s'\, dz, \tag{13}$$

where $u_m = 0.22$ at $z = 18$, and λ is a constant of order one, which we find from the best fit of the LES data. Figure 6b displays the theoretical dependence of the penetration height obtained by integrating Eq. (13) with $\lambda = 0.8$. The comparison with the LES results indicates that the penetration height is well predicted at low Froude numbers but overestimated at the largest Fr. To explain this, we recall that the rising height of weak fountains in a homogeneous fluid scales as Fr^2, whereas that of forced fountains (where the turbulent entrainment is taken into account) scales with Fr. The largest Froude numbers investigated here correspond to the transition between the weak and forced regime, and therefore Eq. (12) is appropriate, for the weak regime overestimates the penetration height at these Froude numbers.

Note that the theory based on the conservation equations by Morton et al. (1956) is not expected to be valid for weak fountains near the thermocline because the basic assumptions of the model about self-similarity and constant turbulent entrainment do not hold. Our calculations show that this model significantly underestimates the penetration heights from the LES.

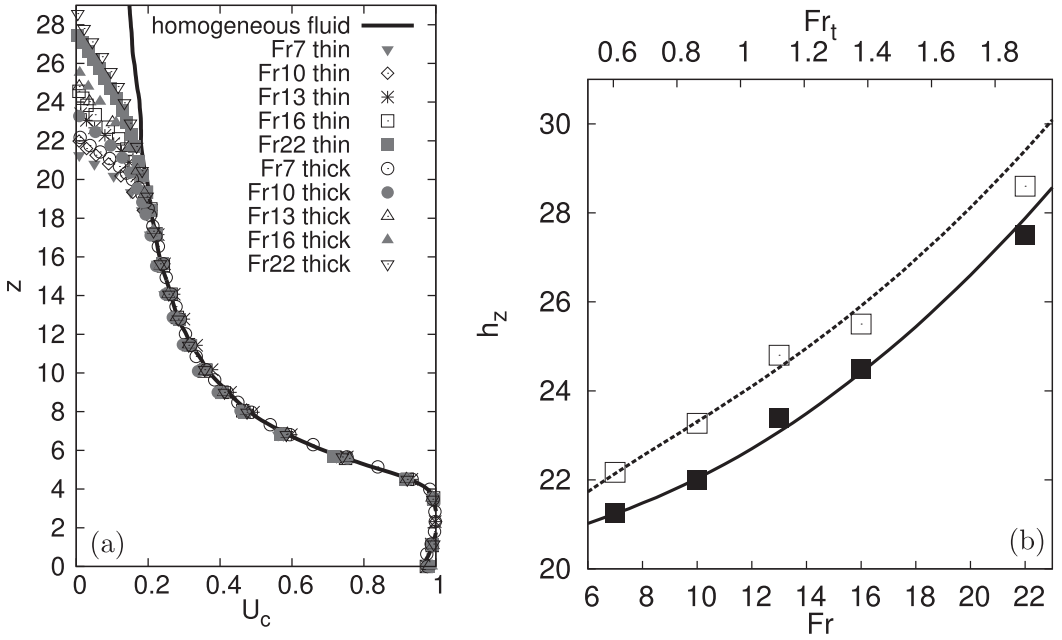

FIG. 6. (a) Mean centerline velocities for the jet in a homogeneous fluid and for all the simulations in the stratified media indicating mean jet penetration. (b) Theoretical prediction of the mean penetration height vs the Froude number: $\gamma = 2$ (solid) and 0.5 (dashed). Symbols ■ and □ denote the mean heights obtained in the simulations for $\gamma = 2$ and 0.5, respectively.

The dashed lines in Fig. 5 indicate the boundaries of the thermocline (they correspond to 10% and 90% of the temperature jump) obtained from the average temperature field. It can be seen that for the thin thermocline and small Froude number (Fig. 3a), the temperature jump is deformed as an entire structure reminiscent of a thick membrane, with variations of the height of the upper and lower boundaries only in the region of the jet impingement; a strong stratification dampens turbulence and inhibits mixing. For the higher Froude numbers (Figs. 5b,c) the thin thermocline is significantly deformed, revealing a toroidal well-mixed region adjacent to the jet. The size and depth of this well-mixed region grow with the Froude number.

Two observations can be made here: First, this behavior is consistent with the experimental observations for a turbulent jet impinging on a stratified interface [see, for instance, Shy (1995) and Cotel et al. (1997)] where the formation of a large toroidal vortex was observed immediately after the jet impingement and related to the generation of baroclinic vorticity, which tends to push back the interface to the unperturbed state. Second, which might be more relevant to our system, we report that the turbulent regime of weak fountains ($1 \lesssim \mathrm{Fr}_t \lesssim 1.9$), forming at the thermocline, is characterized by vertical oscillations of the jet. Here, the fluid falls down quasi periodically from the top (Troitskaya et al. 2008; Burridge and Hunt 2012; Druzhinin and Troitskaya 2013); these oscillations are not necessarily axisymmetric, although their average is. The fluid falling from the top forms the vortical structures adjacent to the jet at the lower boundary of the thermocline. These structures, together with the small-size eddies on the jet shear layers crossing the thermocline, are responsible for the turbulent mixing. These large structures and the small eddies on the shear layer are illustrated by the instantaneous fields of temperature and vertical velocity shown in Fig. 7 for both stratifications and Fr = 7 and 22 (i.e., $\mathrm{Fr}_t = 0.6$ and 1.9).

The effect of the fountain oscillatory dynamics on the generation of internal waves in the thermocline will be discussed in the next section.

To substantiate these observations, we study the change of the level of neutral buoyancy with increasing Froude number, that is, the level where the jet spreads horizontally, forming a gravity current. This is illustrated by the mean horizontal velocity profiles at the distance $r = 20$ from the jet center (Fig. 8a). The vertical coordinate in this picture is $\eta = \gamma(z - z_p)$, so that the origin is moved to the thermocline center and $\eta = \pm 1$ correspond to the thermocline boundaries. Note that the width of the horizontal flow is determined by the radius of the jet at the thermocline entrance, which is the same for the two values of thermocline thickness used. In other words, the different width of the flows in Fig. 8a reflects the different ratio between the thermocline

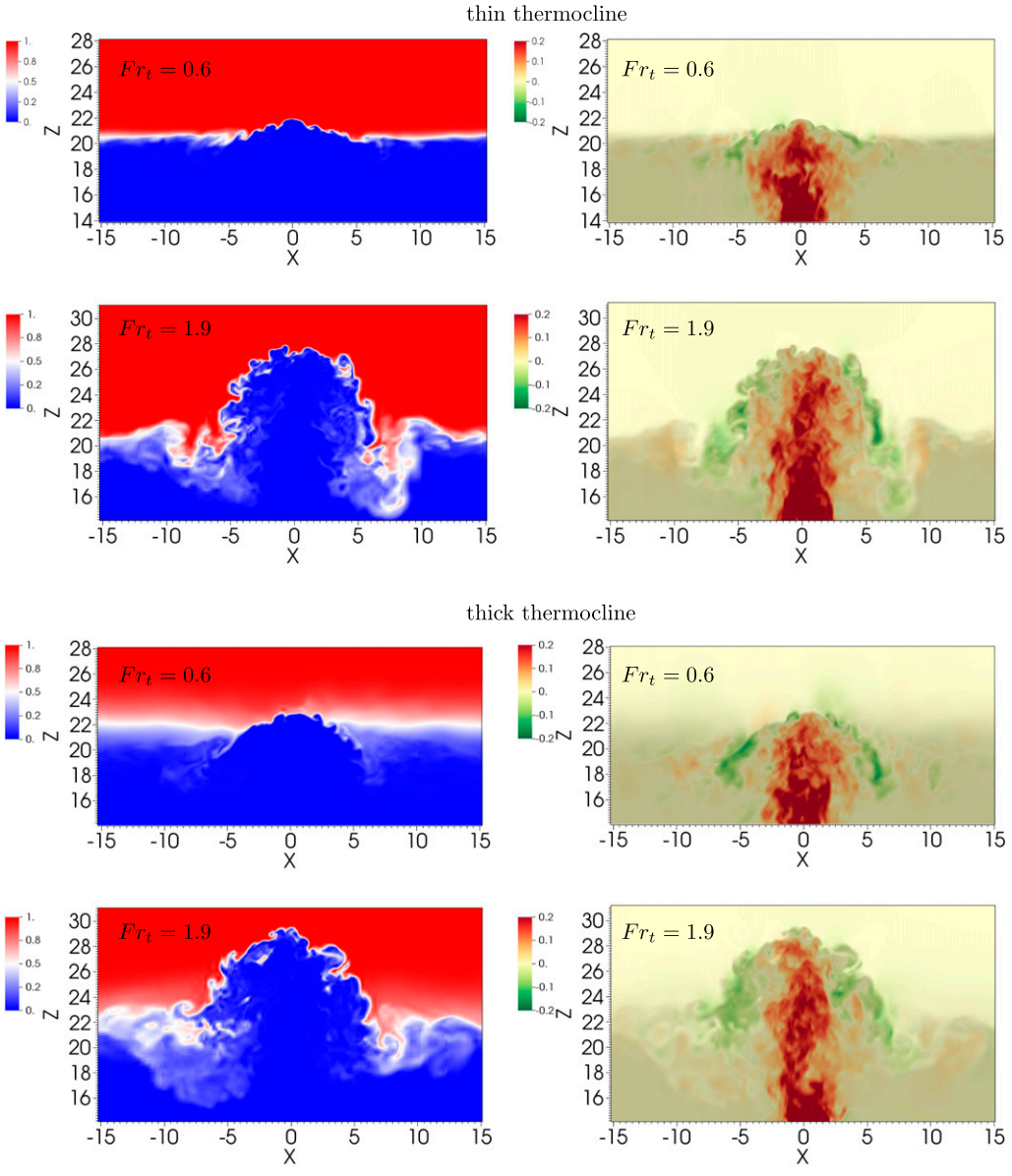

FIG. 7. The (left) instantaneous temperature and (right) vertical velocity fields in the thermocline for both stratifications.

width and the radius of the impinging jet. For small Froude numbers, the level of neutral buoyancy is below the lower thermocline boundary while it is moving higher up into the thermocline for larger Froude numbers, indicating a better mixing with the fluid in the thermocline and from the upper layer of stratification.

To quantify mixing, we calculate the mean temperature of the horizontal flow through the cylindrical surface of radius $r = 20$ surrounding the jet; this distance is chosen so that the control volume is far enough from the mixing region adjacent to the jet (see Fig. 5, $15 < z < 25$). Using the mean volume and mass fluxes of the gravity current, we obtain the following expression for the averaged temperature of the gravity current:

$$T_{\mathrm{gr}} = \frac{\int T U_{\mathrm{hor}}\, dz}{\int U_{\mathrm{hor}}\, dz}, \tag{14}$$

where we perform the integration over the region characterized only by positive values of U_{hor}; that is, we consider the flow propagating outwards from the jet (detrainment) and do not account for entrainment. The

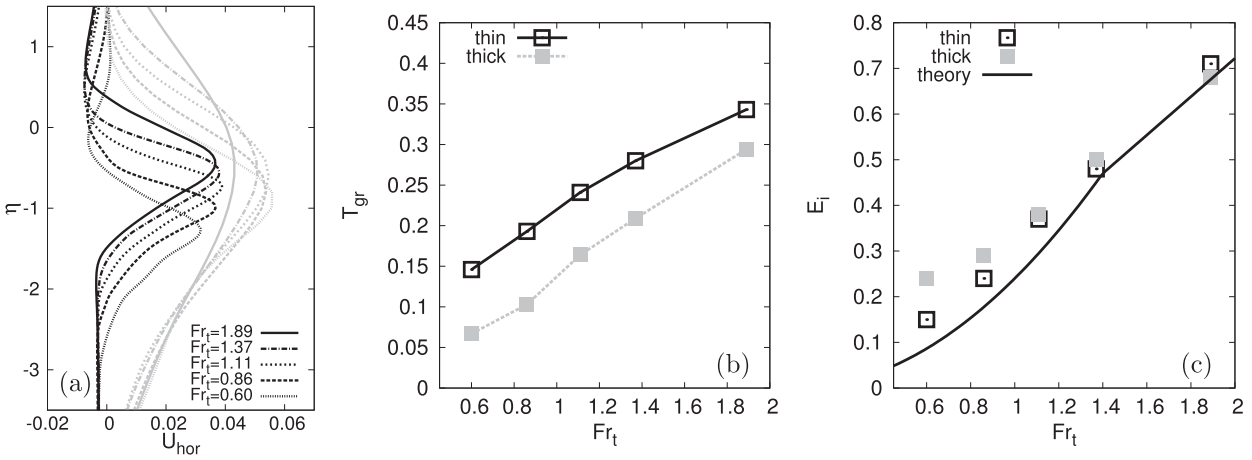

FIG. 8. (a) Velocity profiles of the gravity currents propagating at the level of neutral buoyancy at a distance $r = 20$ from the jet axis (gray curves indicate thin thermocline and black curves indicate thick thermocline). (b) Average temperature of the gravity current as a function of the thermocline Froude number. (c) Entrainment flux obtained from Eq. (17) as a function of the thermocline Froude number.

values obtained are displayed in Fig. 8b to demonstrate that the average temperature of the horizontal flow increases with the Froude number, again indicating a better mixing with the fluid in the thermocline and the upper layer of stratification.

To study the mixing at the thin and thick thermoclines, we introduce the entrainment flux $E_i = Q_e/Q_{\text{in}}$, similarly to the definition used for investigations of turbulent entrainment by jets and plumes in two-layer (sharp interface) stratified fluid (Shy 1995; Cotel et al. 1997; Shrinivas and Hunt 2014, 2015). When the jet penetrates into the upper layer of stratification, it forms a domelike structure, which entrains the ambient fluid. Thus, Q_e in the definition above is the volume flux of the fluid entrained by the jet top and Q_{in} is the volume flux of the fluid in the jet at the interface between the two layers of stratification. This domelike structure is reported in Fig. 9, where we show the mean horizontal velocity where the jets interact with the thermocline for both stratifications under consideration. Since we have a smooth change of temperature between the two layers, the "dome" over which the fluxes are computed is depicted by the black lines in Fig. 9; we consider a closed surface consisting of a circular cylinder cut on the lower side along the surface of the fountain. As the total volume flux is equal to 0, we can estimate the flux through the dome perimeter Q_e as the sum of the fluxes through the cylinder top and side Q_{cyl}:

$$Q_{\text{cyl}} = 2\pi R \int_{z_1}^{z_2} u_{\text{side}}\, dz + 2\pi \int_0^R u_{\text{top}} r\, dr, \qquad (15)$$

where u_{side} and u_{top} are the velocities normal to the side and top surfaces of the cylinder, respectively; z_1 and z_2 are the vertical coordinates corresponding to the bottom and top of the cylinder; and R is the radius of the base of the cylinder.

We define the inflow volume flux Q_{in} as the volume flux of the jet at the level $z = 18$, where it is the same for all the cases considered here (see Fig. 6a):

$$Q_{\text{in}} = 2\pi \int_0^{\infty} u_{\text{in}} r\, dr, \qquad (16)$$

with u_{in} as the vertical velocity. The entrainment flux can finally be written as

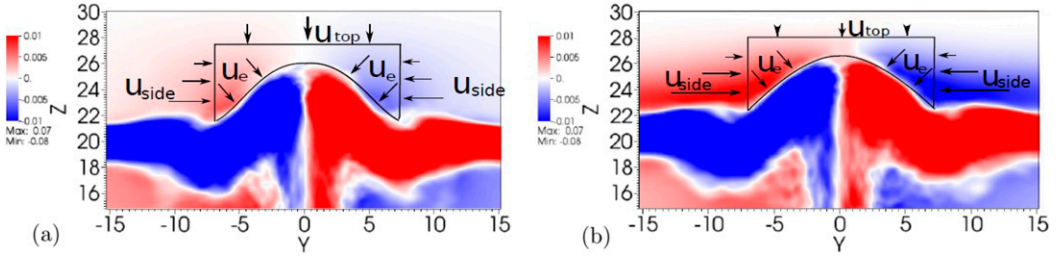

FIG. 9. Mean horizontal velocity fields in the jet impinging on the thermocline for Fr = 16 ($\text{Fr}_t = 1.37$): (a) thin thermocline and (b) thick thermocline.

$$E_i = \frac{R\int_{z_1}^{z_2} u_{\text{side}}\, dz + \int_0^R u_{\text{top}} r\, dr}{\int_0^\infty u_{\text{in}} r\, dr}. \quad (17)$$

The dependence of the entrainment flux on the Froude number at the thermocline entrance is displayed in Fig. 8c, where the dashed curve indicates the theoretical entrainment flux for a jet in an unconfined medium in the limit of small Froude numbers ($\text{Fr}_t < 1.4$) and a sharp interface, $E_i = 0.24\text{Fr}_t^2$, together with the approximation of the theoretical curve for larger Froude numbers, both taken from Shrinivas and Hunt (2014). This power law is obtained from an energy balance: a fraction of the kinetic energy supplied by the jet at the interface per time unit is expended into work (per time unit) against the gravity force to entrain fluid from the upper stratification over a distance of the order of the jet scale at the thermocline entrance, yielding $Q_e/Q_i \sim u_t^2/R_t\Delta g \sim \text{Fr}_t^2$ (here u_t and R_t are the mean jet velocity and radius taken at the level of the density interface). The value of the constant $A = 0.24$ is obtained theoretically by Shrinivas and Hunt (2014).

Our data follow the quadratic law obtained in Shrinivas and Hunt (2014) for the thin thermocline; however, the entrainment rate is slightly higher. Owing to the smoother temperature change in the thermocline, the turbulent transfer is expected to be more active in this case than for the sharp interface.

At small Froude numbers, the fountain in the thick thermocline entrains more fluid, although the average temperature of the horizontal gravity current is lower. This is because the jet does not penetrate through the thermocline up to the warm upper layer. At the same time the stratification is weaker, which results in a larger surface of the dome and more efficient turbulent transfer. At higher Froude numbers, when the jet penetrates through the thermocline, the entrainment fluxes are rather close for the two cases, but the average temperatures for the thick thermocline are lower.

We explain this difference through the presence of a horizontal flow toward the jet in the upper part of the thick thermocline. In fact, we recall that entrainment velocities (denoted as secondary flows; Shrinivas and Hunt 2015) play an important role in the process of confined entrainment at small Froude numbers. As shown in Fig. 9a, the flow above the dome in the thin thermocline looks similar to the model of a thin "vortex sheet" on the dome perimeter for unconfined entrainment in a two-layer stratification (Shrinivas and Hunt 2014). Interestingly, a horizontal secondary flow appears in the thick thermocline. Figure 9b shows a two-layer horizontal flow in the thermocline. In this case, stratification inhibits vertical turbulent transfer and the jet entrains the fluid from the upper thermocline, forming a well-pronounced horizontal secondary flow over the initial gravity current. Even for the largest penetration heights of the jet investigated here, the structure of the horizontal flow essentially does not change and the jet entrains fluid mostly from the thermocline, not from the upper stratification layer as in the case of the thin thermocline.

Finally, note that the thick thermocline conditions correspond to the experimental setup used in Troitskaya et al. (2008) and Bondur et al. (2010) to investigate turbulent jets and plumes in a thermocline-like stratified tank. The horizontal velocity profiles measured in the experiments at a distance $24R_t$ from the jet center display a backflow from 6% to 15% of the maximal velocity of the gravity current in the upper thermocline. Our simulations give a magnitude of 15%–20% at a closer distance of $10R_t$.

b. *Generation of internal waves*

In all the simulations, as in the experiments of Troitskaya et al. (2008) and Ezhova et al. (2012), we observe oscillations of the jet top at the thermocline, which results in the generation of internal waves. An example of the instantaneous temperature field at the center of the thermocline and the corresponding isotherms at the distance $r = 20$ from the jet center is shown in Fig. 10 for the case of the thin thermocline Fr = 10, 22 ($\text{Fr}_t = 0.86, 1.9$). The top figure, pertaining to the lower Froude number, displays rather regular waves emanating from the jet and almost sinusoidal isotherms. The plots for the larger Froude number show a more chaotic behavior, the isotherms displaying signs of wave breaking in the thermocline.

The analysis of the dynamics of the jet in the thermocline and of the internal waves is based on the power spectra of the temperature oscillations, $\mathscr{S}(f)$. We consider the isotherm at the center of the undisturbed thermocline $T = 0.5$ and investigate its displacement at several points close to the jet center and far from it. The spectra of the jet oscillations, $z - z_p$ with z_p as the average height of the thermocline $T = 0.5$, are obtained by averaging data from five locations: one in the center of the jet and four from the points on the circle of radius 1.5 (see section 2c). The spectra of internal waves, instead, are obtained by averaging spectra from eight locations at distance $r = 20$ from the jet center. The spectra for Fr = 13 are shown as thin and thick thermoclines in Figs. 11b and 11c as an example. It can be seen that the jet generates internal waves with pronounced spectral peaks.

We first note that all the spectra of the jet oscillations in both stratifications have two peaks. This is consistent

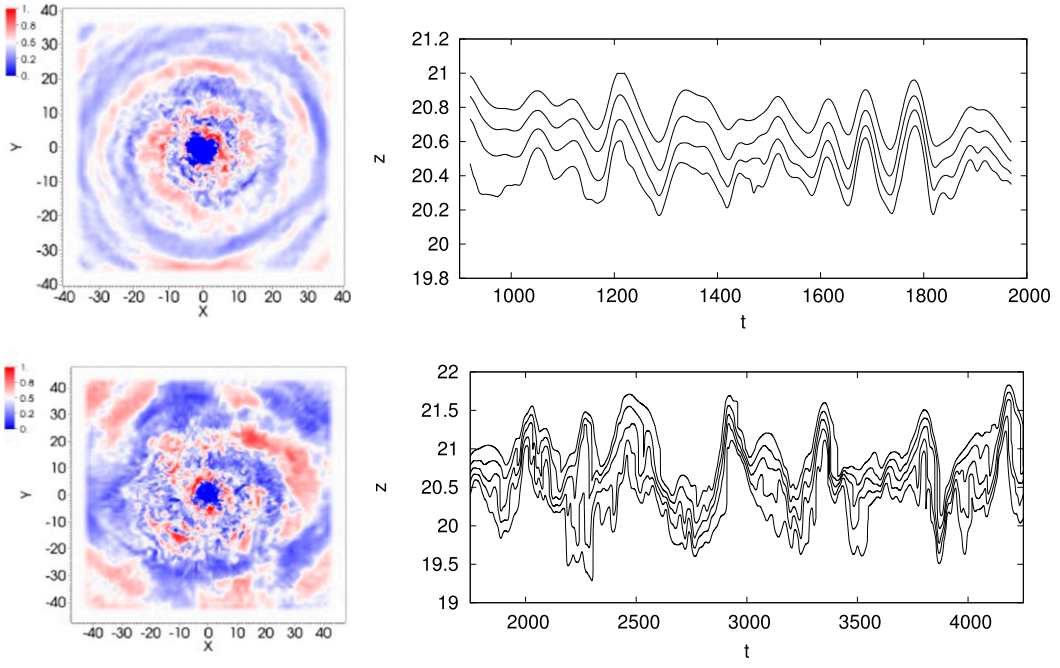

FIG. 10. (left) Instantaneous temperature field in the horizontal plane at the center of the thermocline and (right) time history of the isotherms at distance $r = 20$ from the jet center. (top) The data pertain to the simulation of the thin thermocline with Fr = 10 ($\mathrm{Fr}_t = 0.86$) (isotherms corresponding to temperatures from $T = 0.4$ to 0.7) and (bottom) the simulation with the Fr = 22 ($\mathrm{Fr}_t = 1.89$) (isotherms from $T = 0.3$ to 0.7).

with the observation of fountains in a homogeneous fluid where two peaks have been reported for all cases by Burridge and Hunt (2013). Moreover, for fixed Fr, the spectra of the jet oscillations have peaks at similar frequencies in different stratifications, as shown in Fig. 11a. Thus, the frequencies of the oscillations do not depend on the thermocline thickness for the parameters chosen in the simulations. Note, however, that one expects differences in frequencies when the jet does not penetrate through the thermocline since its effective Froude number is defined by the temperature difference between the lower stratification layer and the level to which the jet penetrates, rather than by the difference between upper and lower stratification. In our case, this difference is probably too small to be detected. Simulations at even lower Fr may possibly reveal this effect.

The frequencies of the spectral peaks for jet oscillations and internal waves are summarized in Table 2 and displayed in Fig. 12. Since the peaks in the spectra are rather wide, we used the following expression to define the main frequencies in the spectra:

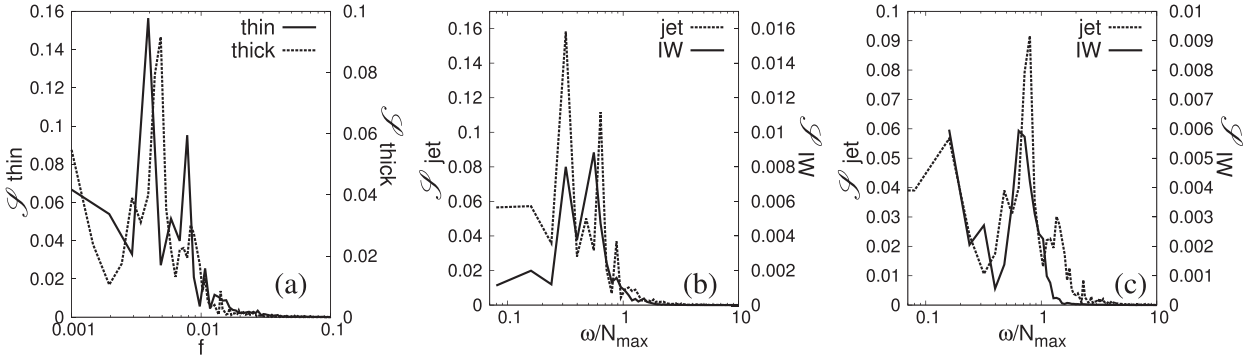

FIG. 11. (a) The spectra of jet oscillations in the thin (solid) and thick thermocline (dashed) for Fr = 13 ($\mathrm{Fr}_t = 1.11$)). (b) The spectra of jet oscillations (dashed) and internal waves (solid), thin thermocline. (c) The spectra of jet oscillations (dashed) and internal waves (solid), thick thermocline.

TABLE 2. Frequencies of jet oscillations and internal waves in the thin and thick thermoclines.

Fr (Fr$_t$)	$\hat{f}_{1\text{jet}}$ thin	$\hat{f}_{2\text{jet}}$ thin	$\hat{f}_{1\text{jet}}$ thick	$\hat{f}_{2\text{jet}}$ thick	$\hat{f}_{1\text{IW}}$ thin	$\hat{f}_{2\text{IW}}$ thin	$\hat{f}_{1\text{IW}}$ thick
7 (0.60)	0.0096	0.0179	0.0098	0.0177	0.0100	0.0173	0.0083
10 (0.86)	0.0072	0.0146	0.0068	0.0152	0.0078	0.0135	0.0063
13 (1.11)	0.0038	0.0082	0.0042	0.0084	0.0040	0.0073	0.0045
16 (1.37)	0.0024	0.0055	0.0026	0.0054	0.0037	—	0.0030
22 (1.89)	0.0017	0.0048	0.0021	0.0048	0.0023	—	0.0025

$$\hat{f} = \frac{\int_{f_{\min}}^{f_{\max}} f\mathscr{S}(f)\,df}{\int \mathscr{S}(f)\,df}, \tag{18}$$

where $f_{\min}$ and $f_{\max}$ denote the range of frequencies corresponding to each spectral peak. The figure shows a decrease in the frequency of the oscillations with the Froude number in agreement with the fountains in a homogeneous medium (Burridge and Hunt 2013).

For the three smallest Froude numbers, the spectra of jet oscillations have a pronounced large peak and a second small peak at approximately double the frequency. For the two highest Froude numbers investigated, the peaks have approximately equal magnitude. The spectra of internal waves are different at lower Froude numbers, with two peaks in the thin thermocline and one peak in the thick thermocline, primarily due to the difference in the maximal buoyancy frequencies as explained below.

Indeed, the thickness of the two thermoclines considered in this paper corresponds to a factor of 2 difference in the maximal buoyancy frequency. The dimensionless buoyancy frequency $N^2 = ga_T(dT_s/dz)$ can be rewritten in our case as

$$N^2 = \frac{0.5\gamma}{\mathrm{Fr}^2}\frac{1}{\cosh^2[\gamma(z - z_p)]}. \tag{19}$$

Thus, $N_{\max} = 1/\mathrm{Fr}$ and $N_{\max} = 0.5/\mathrm{Fr}$ for $\gamma = 2$ and 0.5, respectively. The spectra of jet oscillations and internal waves for the same Fr = 13 and different stratifications are shown in Figs. 11b and 11c. The spectra of jet oscillations have two distinct peaks, the higher one possibly corresponding to the harmonics of the lower. The thin thermocline has a larger maximal buoyancy frequency, which allows the propagation of waves of both frequencies (first and second peak), while only the lowest-frequency perturbation can generate internal waves at the thick thermocline. Figure 12b clearly indicates the frequency cutoff due to the smaller maximal buoyancy frequency, since the second frequency in the spectra of the jet oscillations is always higher than the maximum buoyancy frequency for the thick thermocline.

For the two higher Froude numbers, the spectra of internal waves have one pronounced peak close to the lower peak of the jet oscillations, which is surprising in case of the thin thermocline where one expects propagating waves at both frequencies. The simulations for these cases, when the jet penetrates far enough through

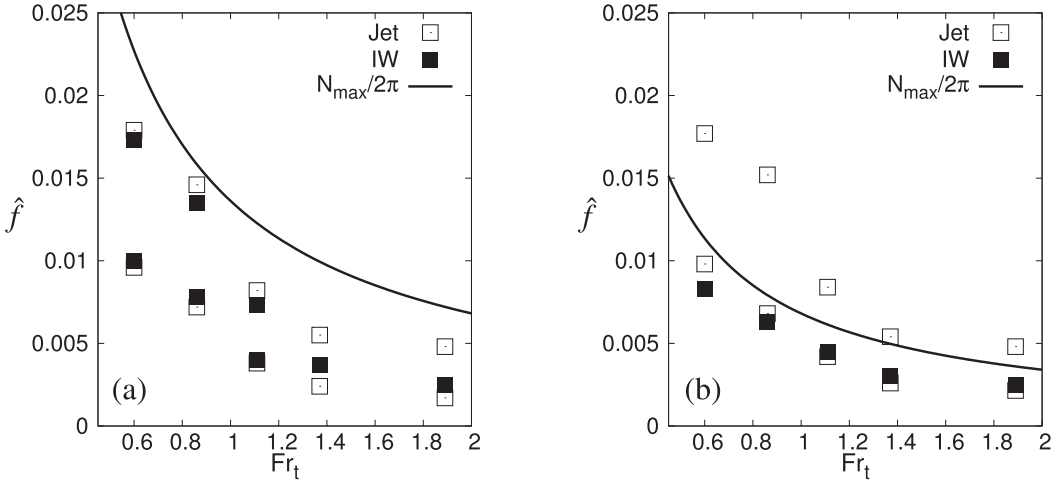

FIG. 12. The frequencies of the jet oscillations and internal waves as the functions of the Froude number: (a) thin thermocline and (b) thick thermocline. The solid curves correspond to the maximal buoyancy frequency.

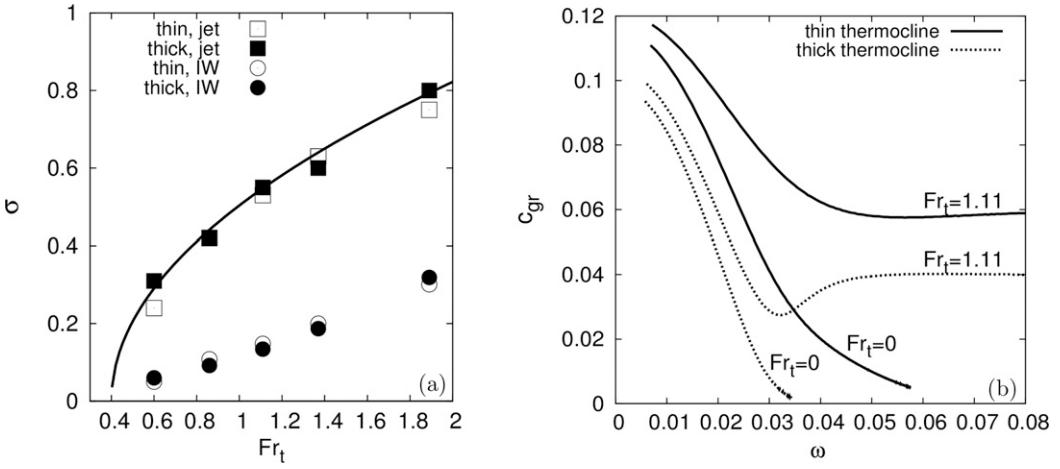

FIG. 13. (a) The amplitudes of the jet oscillations and the internal waves as function of the thermocline Froude number. Solid line represents the stationary solution of Landau equation. (b) The group velocity of the first mode of internal waves as a function of frequency.

the thermocline, show that fluid falling from the jet top loses axial symmetry, in contrast to the cases at smaller Froude numbers, and the jet undergoes ''tilting'' from one side to the other. This may explain why internal waves propagate only at the low frequency. Moreover, the fluid falling from the fountain goes deep to the lower layer of stratification and then bounces back, creating additional disturbances in the thermocline, which might result in a frequency shift. This is more relevant for the thin thermocline where we see a more pronounced shift of the frequency of the internal waves from the lower peak in the spectra of the jet oscillations (Fig. 12a).

In case of the thin thermocline, the frequency of the higher peak in the spectra of the internal waves decreases from $0.5N_{\max}$ to $0.3N_{\max}$. For the thick thermocline, the peak in the spectrum of the internal waves corresponds to the lower peak in the jet oscillations spectrum and is close to $0.7N_{\max}$ for all the simulations. The latter is consistent with the results of the experiment by Ezhova et al. (2012), where the oscillations of a turbulent jet in a stratified fluid and the corresponding internal waves have been investigated. As mentioned before, the jet diameter at the thermocline entrance was of order of the thermocline thickness in these experiments corresponding to our simulations with the thick thermocline $\mathrm{Fr}_t \sim 1$. In the experiments, the jet oscillations are characterized by pronounced peaks close to $0.7N_{\max}$ and at the frequency close to the maximum buoyancy frequency. Internal waves have been revealed at the frequencies $0.7N_{\max}$ in agreement with our simulations.

The root-mean-square σ of the isotherms both for jet oscillations and internal waves, that is, close and far from the jet axis, is obtained from the power spectra $\mathscr{S}(f)$,

$$\sigma = \left[\int \mathscr{S}(f)\, df\right]^{1/2}, \tag{20}$$

and is used to characterize the amplitudes of the oscillations. The amplitudes of the jet oscillations and internal waves are displayed in Fig. 13a versus the Froude number for both stratifications. Interestingly, the amplitudes of the jet oscillations and of the internal waves are close to each other in both cases, although the work against the gravity force to obtain the same amplitude is larger in the thin thermocline as the density gradient is higher. This suggests that the waves are transmitted more effectively in the case of the thin thermocline, probably because for the thick thermocline the wave frequency is close to the maximal buoyancy frequency.

The amplitude of the jet oscillations follows the stationary solution to the Landau equation

$$\frac{d\sigma}{dt} = \sigma[\mu(\mathrm{Fr}_t - \mathrm{Fr}_{t0}) - \beta\sigma^2], \tag{21}$$

describing the soft excitation of self-sustained oscillations (μ and β are free parameters here), with $\mathrm{Fr}_{t0} = 0.4$, $\mu/\beta = 0.42$ based on the best fit of the experimental data. This is consistent with the experimental and numerical results obtained for a jet interacting with a pycnocline (Troitskaya et al. 2008; Druzhinin and Troitskaya 2013). The investigation of the stability of the experimentally measured velocity profiles of the fountain in the pycnocline by Troitskaya et al. (2008) and Ezhova and Troitskaya (2012) reveals a finite region of absolute

instability along the jet, thus fulfilling a necessary condition for self-sustained oscillations of the flow. It has been demonstrated that the frequency of self-sustained oscillations is in agreement with the results of the linear stability analysis of the flow in the thermocline. The present simulations for the thick thermocline follow the experimental setup of Ezhova and Troitskaya (2012), and the LES results are consistent with the experiment. Hence, we can conclude that the generation of internal waves results from the self-sustained excitation of the jet oscillations in the thermocline.

We investigate the vertical structure of the internal waves and quantify their energetics. The energy flux of the internal waves in the presence of an inhomogeneous horizontal flow, as we have in this case because of the horizontal gravity flow, is calculated following Kamenkovich and Monin (1978). The equations of motion linearized around a horizontal mean flow in cylindrical coordinates are

$$\frac{Du_r'}{Dt} + u_z' \frac{dU_{\text{hor}}}{dz} + \frac{1}{\rho_0}\frac{\partial p'}{\partial r} = 0, \tag{22}$$

$$\frac{Du_\phi'}{Dt} + \frac{1}{\rho_0}\frac{1}{r}\frac{\partial p'}{\partial \phi} = 0, \tag{23}$$

$$\frac{Du_z'}{Dt} + g\frac{\rho'}{\rho_0} + \frac{1}{\rho_0}\frac{\partial p'}{\partial z} = 0, \tag{24}$$

$$g\frac{D(\rho'/\rho_0)}{Dt} - N^2(z)u_z' = 0, \quad \text{and} \tag{25}$$

$$\nabla \cdot \mathbf{u}' = 0, \tag{26}$$

where $D/Dt = \partial/\partial t + U_{\text{hor}}\partial/\partial r$. $\mathbf{U}_{\text{hor}} = U_{\text{hor}}\mathbf{r}$ is the mean flow and $\mathbf{u}'$ denotes the small perturbations of the mean flow.

The equation for energy conservation can be obtained by multiplying Eq. (22) with u_r', Eq. (23) by u_ϕ', and Eq. (24) by u_z' and summing. From Eq. (25), taking into account that $u_z' = D\xi/Dt$, we find that $g\rho' = \rho_0 N^2(z)\xi$ (where ξ is the vertical displacement of a fluid particle).

Finally, the equation of the wave energy conservation reads

$$\frac{\partial E}{\partial t} + \nabla \mathbf{F} = -I, \tag{27}$$

where the wave energy E, the energy flux $\mathbf{F}$, and the production/dissipation term I are

$$E = \frac{1}{2}\rho_0(\mathbf{u}'^2 + N^2\xi^2), \tag{28}$$

$$\mathbf{F} = \mathbf{U}_{\text{hor}}E + \mathbf{u}'p', \quad \text{and} \tag{29}$$

$$I = \rho_0 u_r' u_z' \frac{dU_{\text{hor}}}{dz}. \tag{30}$$

The quantity I describes the interaction of the mean flow with the wave. From Eq. (27) it follows that the integral wave energy flux is not conserved due to this term. In the present configuration, waves can grow or decay in space where $\partial E/\partial t$ is zero at statistically steady state.

The surface-integrated value of the wave energy flux at the distance r from the jet axis is normalized with the energy flux of the jet at the thermocline entrance:

$$\frac{F}{F_{\text{jet}}} = \frac{R\int_{z_1}^{z_2}\left[\frac{1}{2}(\mathbf{u}'^2 + N^2\xi^2)U_{\text{hor}} + \frac{p'u_r'}{\rho_0}\right]dz}{\frac{1}{2}\int_0^\infty U_t^3 r\,dr}. \tag{31}$$

We measure the profiles of the energy flux at four radial points and averaged them to get the final profile. The inflow energy flux is taken at the level $z = 18$. The profiles F/F_{jet}, pertaining to the thick and thin thermocline at the distances $r = 20$ and 25, are shown in Fig. 14. It can be seen that the energy does not only decay with the distance from the jet center, but the profiles are also deformed, especially in the areas affected by the shear due to the horizontal flow, presumably due to the enhanced decay resulting from the interaction with the mean flow.

The surface-integrated wave energy flux normalized with the jet energy flux is displayed in Fig. 15 versus the Froude number. The difference between the values at $r = 20$ and 25 illustrates the difference in the decay of the energy of the internal waves due to the interaction with the mean flow. Note that the wave energy flux is around 4%–5% of the energy of the jet for the thin thermocline and is almost half for the thick thermocline. This can be partly explained by the fact that the counterflow in the upper thermocline transfers energy in the opposite direction, that is, toward the jet. The whole flux, however, is always positive. Note also the jump in the energy flux for the largest Froude number when the horizontal flow occupies more space in the thermocline, preventing the transfer of energy toward the jet.

We finally comment on the difference in the velocities of wave propagation. As explained above, transients in the simulations are very different when changing the thickness of the thermocline, and the difference in the domain size (40 from the jet center to the lateral boundary along the axes for the thin thermocline and 47 for the thick thermocline) is too small to explain this. The fact that the internal waves are significantly slower in the thick thermocline can be related to the dispersion properties of the internal waves. The dispersion relation for the waves $\Psi \sim \psi(z)e^{-i\omega t + ikr}$ in a stratified medium is obtained from the solution of the eigenvalues of the Taylor–Goldstein equation:

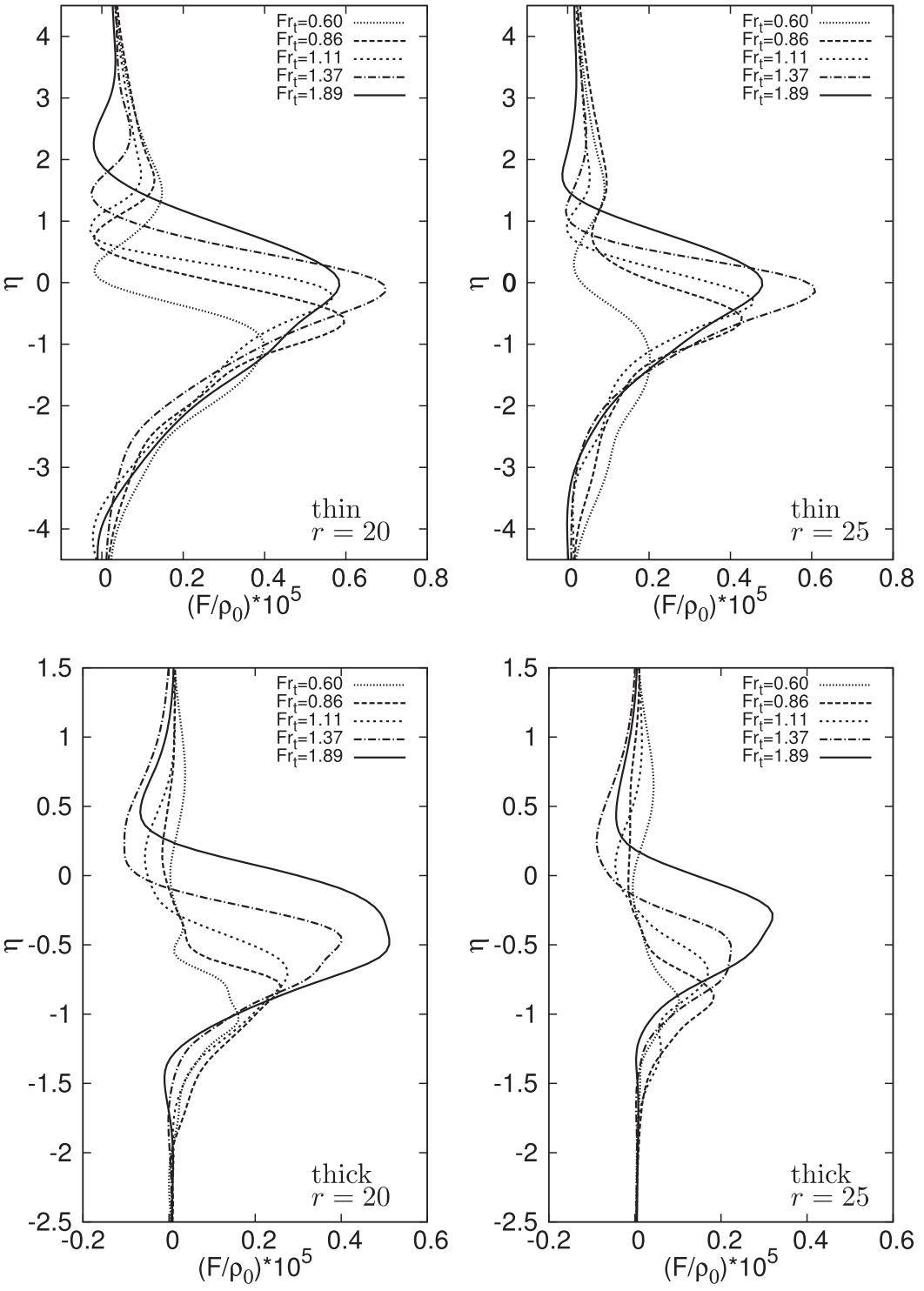

FIG. 14. Vertical profiles of the energy flux of internal waves: (top) thin thermocline and (bottom) thick thermocline. (left) $r = 20$ and (right) $r = 25$.

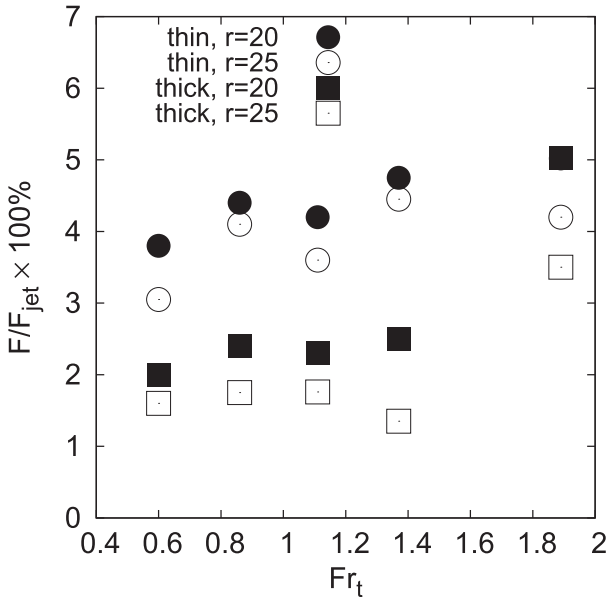

FIG. 15. The surface-integrated wave energy flux normalized with the jet energy flux at the entrance to the thermocline. The values at the largest Froude number for the distance $r = 20$ coincide.

$$\frac{d^2\psi}{dz^2} + \left[\frac{N^2}{(U_{\rm hor}-c)^2} - \frac{(U_{\rm hor})''_{zz}}{U_{\rm hor}-c} - k^2\right]\psi = 0,$$
$$\psi(H_d) = \psi(H_u) = 0, \qquad (32)$$

where ψ is a streamfunction, N is the buoyancy frequency, $U_{\rm hor}$ is the mean horizontal velocity that depends on the vertical coordinate z, $c = \omega/k$ is the wave phase velocity (ω is the wave frequency and k is the wavenumber), and $z = H_u$, H_d denote the locations of the upper and lower boundaries [Eq. (32) is made nondimensional with U_0 and D_0]. This eigenvalue problem is solved numerically for the stratification profiles and the horizontal velocities extracted from the simulations.

The group velocity $c_{\rm gr} = d\omega/dk$ of the first (fundamental) mode of the internal waves is displayed in Fig. 13b for the Froude numbers Fr = 0 (no flow) and Fr = 13 (with horizontal flow) and both stratifications. Similar conclusions apply to higher modes. Note the significant change in the group velocities in the presence of the horizontal flow due to the jet intrusion at the level of neutral buoyancy. In particular, we find waves with frequencies higher than the maximal buoyancy frequency that propagate with group velocities approaching the maximal velocity of the horizontal gravity flow. The largest fluctuations associated with these modes are localized in the flow as compared to the lower-frequency modes localized in the thermocline. For the internal waves at Fr = 13 (see the frequencies in Table 2) we estimate the group velocities of the fundamental modes to be $c_{\rm gr} = 0.04$ for the thick thermocline and $c_{\rm gr} = 0.08$ for the thin thermocline, which explains the difference in time needed to reach a statistically steady state: $t_{d,\rm thin} = 1000$ time units and $t_{d,\rm thick} = 1800$ time units.

4. Conclusions

We have presented the results of numerical simulations of a turbulent jet interacting with a thermocline in an unconfined stratified medium. Two stratifications have been modeled: a thin and a thick thermocline, with thickness smaller and of the order of the jet diameter at the thermocline entrance. The simulations have been performed for five Froude numbers in each stratification, ranging between 0.6 and 1.9, values typical of engineering and geophysical flows (such as submerged buoyant jets from wastewater outfalls).

We show that the jet mean penetration height can be well predicted from the conservation of the source energy of a turbulent jet in a thermocline (Kaye and Hunt 2006), valid for weak fountains.

The entrainment flux in the thin thermocline, related to the turbulent mixing of the jet with the surrounding medium, is consistent with the theoretical model developed for the case of a jet impinging at a sharp interface. At small Froude numbers, the entrainment is more effective in the thick thermocline, but already at $\mathrm{Fr}_t \approx 1$ the fluxes become equal for both stratifications. There is an important difference, however, in the average secondary flows for the two stratifications. For the thin thermocline the entrainment velocity is approximately the same around the dome formed by the jet penetrating through the thermocline. The entrainment in the thick thermocline, instead, is mostly from the sides of the dome due to a pronounced horizontal flow in the upper thermocline, with only a small part of fluid coming from the upper stratification layer. This difference is observed over the whole range of Froude numbers investigated here, even in the case when the jet penetrates through the thick thermocline.

The fountain formed by the jet penetrating into the thermocline oscillates generating internal waves. The amplitudes of the jet oscillations grow with the Froude number as $\mathrm{Fr}_t^{1/2}$ corresponding to the regime of soft self-excitation of the flow. We find two peaks in all the spectra: for the smaller Froude numbers (up to $\mathrm{Fr}_t \approx 1$), the peak at the higher frequency is rather weak as compared to the second one, while at the larger Froude numbers, they are comparable. The frequencies of the jet oscillations at fixed Fr_t are basically the same for both stratifications. These oscillations generate internal waves. The frequencies of the internal waves depend also on the dispersion properties of the stratified medium, and oscillations at frequency exceeding maximal buoyancy frequency are not found in

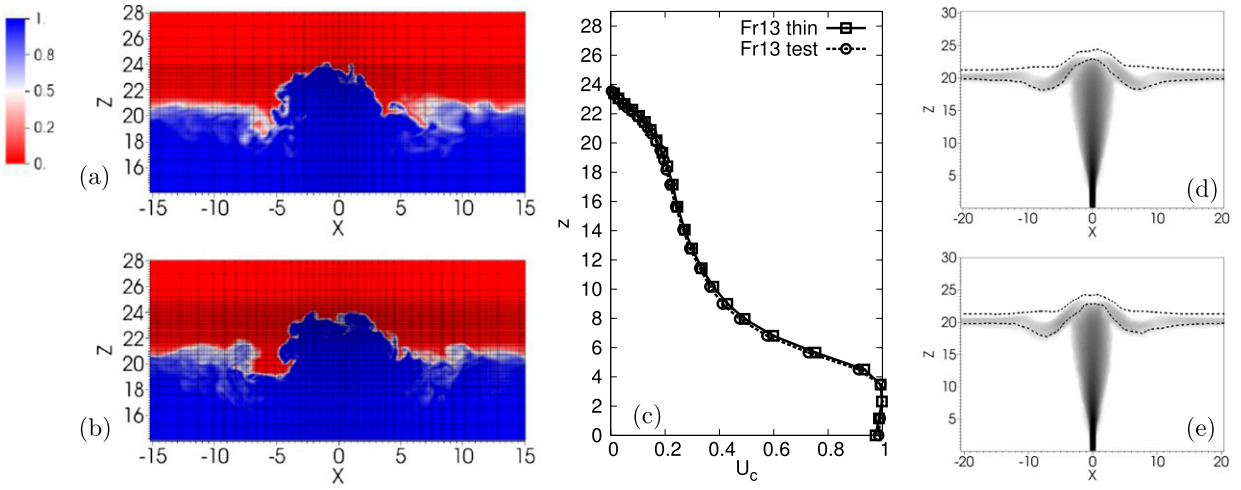

FIG. A1. The mesh and instantaneous temperature fields for Fr = 13 (Fr_t = 1.11), thin thermocline, in (a) the regular simulations and (b) in the validation case. (c) Average centerline velocities for the test case and in regular simulations. Average velocity magnitude (d) in the regular simulations and (e) in the test case. Dashed curves denote the contour lines of average temperature $T = 0.1$ and 0.9.

the spectra of internal waves. Therefore, at the lower Froude numbers both peaks are present in the spectra of internal waves in case of the thin thermocline while only one peak is present in the thick thermocline.

At the higher Froude numbers there is one pronounced peak in the spectra of internal waves corresponding approximately to the lower peak in the spectra of jet oscillations. This is consistent with the results of the laboratory experiments of Troitskaya et al. (2008) and Ezhova et al. (2012), corresponding to our simulations with the thick thermocline at $Fr_t \approx 1$.

The energy flux of internal waves at the thermocline entrance is estimated to be around 4%–5% of the jet energy for the thin thermocline at the distance $r = 20$ from the jet center and almost half for the thick thermocline, except for the largest Froude number $Fr_t = 1.89$, when the fluxes are equal. The energy profiles and estimates of the energy flux at the distance $r = 25$ show that internal waves are significantly influenced by the horizontal gravity flow.

We finally make some remarks regarding a possible application of the present numerical results to the wastewater outfall system. As in the scale laboratory modeling of the real system (Troitskaya et al. 2008), we have observed the jet oscillations resulting in the generation of internal waves at a frequency close to $0.7N_{\max}$ for the thick thermocline cases. These waves can be rather strong with an average amplitude up to 20% of the thermocline thickness (40% peak to peak) at the distance of 10 jet radii at the thermocline from the source. The seasonal change of the pycnocline, as we briefly discussed in the introduction, is characterized primarily by its sharpening and its transition closer to the surface. Therefore, at the entrance to the pycnocline, the diameter of the jet increases and the vertical velocity decreases, that is, increasing γ_t and decreasing the Froude number at the pycnocline entrance. Hence, we expect that in summer, because of the lower Fr_t and amplitude, the internal waves, albeit closer to the free surface, generate less mixing, and the entrainment at the top of the jet is less effective than in winter. The waste water effluent will be located closer to the free surface, and its dilution will be reduced in summer, presenting a larger threat than in winter when a more effective entrainment and larger-amplitude internal waves will contribute to the dilution of the effluent trapped farther away from the free surface. Better dilution is expected either due to the possible wave breaking or due to the effect of enhancement of turbulence in the field of a nonbreaking internal wave (Matusov et al. 1989; Druzhinin and Ostrovsky 2015).

This study focuses on turbulent jets generated from a momentum source of fluid of the same density as the surrounding ambient fluid. The investigation of the applicability of the results discussed in this paper to a turbulent plume with a finite buoyancy flux is underway. However, if the results presented hold for a plume with a finite buoyancy flux, we expect that the different stratification observed in summer and winter in tidewater glaciers in Greenland (Straneo et al. 2011) will dramatically influence the formation and propagation of internal waves in this setting. In particular, in winter, the interface between the top and bottom layers in some of Greenland's fjords is sharp and thinner than in summer (Straneo et al. 2011), and the buoyant plumes forming at the glacier face due to submarine melting are weaker due to a low (or absent) subglacial discharge. Hence, we expect the lower Fr_t and thinner interface observed in

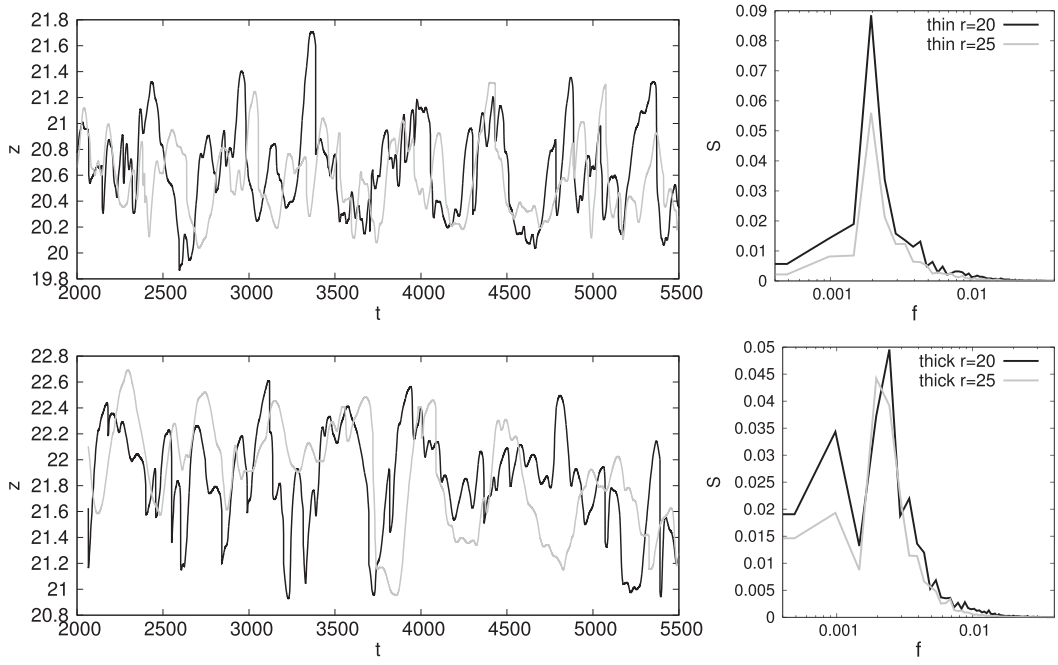

FIG. A2. The examples of the (left) isotherms $T = 0.5$ and (right) average spectra at $r = 20$ and 25 for the (top) thin thermocline and the (bottom) thick thermocline.

winter to generate low-amplitude internal waves with two spectral peaks and the entrainment at the top of the plume to be less effective than in summer when the Froude number is larger. Additionally in summer, given the larger Fr_t and thicker interface, the buoyant plumes interacting with the interface are expected to generate large-amplitude internal waves, which can possibly break and contribute to the dilution of the meltwater plume intruding horizontally at the interface.

Acknowledgments. This work was supported by the Linné FLOW Centre at KTH (E. E.), the European Research Council Grant ERC-2013-CoG-616186, TRITOS (L. B.), and the Swedish Research Council (VR), Outstanding Young Researcher Award (L. B.). Support to C. C. was given by the NSF Project OCE-1434041. Computer time was provided by the Swedish National Infrastructure for Computing (SNIC). Visualization and graphic analysis were performed with VisIt (Childs et al. 2012) and Gnuplot. Subroutines used in the numerical models are available from Numerical Analysis Library of RCC MSU.

APPENDIX

Convergency Test and Additional Validations

We investigate the sensitivity of the simulations to the size of spectral elements. For this aim we perform an additional simulation for $\mathrm{Fr} = 13$, thin pycnocline, with an increased resolution. We left the size of the well-resolved initial region at the inflow ($4 \times 4 \times 10$ spectral elements) unaffected in order to keep the same velocity perturbations and obtain the turbulent jet with the same characteristics. However, we reduce the stretching factor to have 2 times smaller elements at $|x| = |y| = 10$ and reduced the stretching factor along the z axis to have 2 times more elements in the thermocline. The meshes for both cases are shown in Figs. A1a and A1b, displaying as an example the instantaneous temperature fields for both simulations.

Figures A1d and A1e show the average velocity fields together with the thermocline boundaries for both cases, indicating good correspondence. The jet centerline velocity as the function of the vertical coordinate illustrating mean jet penetration is shown in Fig. A1c. The entrainment flux for the test case is $E_{i,\mathrm{test}} = 0.36$, as compared to the regular grid with $E_i = 0.37$. Thus, we may conclude that the simulations converge, and the calculations are resolved enough to get reliable results.

One can investigate the influence of reflections from the boundaries comparing the internal waves measured at the distances $r = 20$ and $r = 25$. We expect to get the weaker signal at $r = 25$ and delay with respect to $r = 20$.

The examples of the isotherms for the largest Froude numbers, as the most critical case for reflections, are shown in Fig. A2 for both stratifications. Figure A2 displays also the averaged spectra of internal waves measured at $r = 20$ and 25 (averaging performed over

eight realizations as explained in section 2b). It can be seen that the signals at $r = 25$ follow the signals at $r = 20$. The average spectra of the isotherms are similar, but the peak for $r = 25$ is lower, thus confirming the absence of reflections from the boundaries at $r = 20$ where we measure internal waves.

REFERENCES

Ansong, J. K., and B. R. Sutherland, 2010: Internal gravity waves generated by convective plumes. *J. Fluid Mech.*, **648**, 405–434, doi:10.1017/S0022112009993193.

——, P. J. Kyba, and B. R. Sutherland, 2005: Fountains impinging on a density interface. *J. Fluid Mech.*, **595**, 115–139, doi:10.1017/S0022112007009093.

Bloomfield, L. J., and R. C. Kerr, 1998: Turbulent fountains in a stratified fluid. *J. Fluid Mech.*, **358**, 335–356, doi:10.1017/S0022112097008252.

——, and ——, 2000: A theoretical model of a turbulent fountain. *J. Fluid Mech.*, **424**, 197–216, doi:10.1017/S0022112000001907.

Bondur, V. G., Y. V. Grebenyuk, E. V. Ezhova, V. I. Kazakov, D. A. Sergeev, I. A. Soustova, and Y. I. Troitskaya, 2010: Surface manifestations of internal waves investigated by a subsurface buoyant jet: Part 2. Internal waves field. *Izv. Atmos. Ocean. Phys.*, **46**, 347–359, doi:10.1134/S0001433810030084.

Burridge, H. C., and G. R. Hunt, 2012: The rise heights of low- and high-Froude-number turbulent axisymmetric fountains. *J. Fluid Mech.*, **691**, 392–416, doi:10.1017/jfm.2011.480.

——, and ——, 2013: The rhythm of fountains: the length and time scales of rise height fluctuations at low and high Froude numbers. *J. Fluid Mech.*, **728**, 91–119, doi:10.1017/jfm.2013.263.

Childs, H., and Coauthors, 2012: VisIt: An end-user tool for visualizing and analyzing very large data. *High Performance Visualization*: *Enabling Extreme-Scale Scientific Insight*, CRC Press, 357–372.

Cotel, A. J., J. A. Gjestvang, N. N. Ramkhelavan, and R. E. Breidental, 1997: Laboratory experiments of a jet impinging on a stratified interface. *Exp. Fluids*, **23**, 155–160, doi:10.1007/s003480050097.

Druzhinin, O. A., and Y. I. Troitskaya, 2012: Regular and chaotic dynamics of a fountain in a stratified fluid. *Chaos*, **22**, 023116, doi:10.1063/1.4704814.

——, and ——, 2013: Internal wave radiation by a turbulent fountain in a stratified fluid. *Fluid Dyn.*, **48**, 827–836, doi:10.1134/S0015462813060136.

——, and L. A. Ostrovsky, 2015: Dynamics of turbulence under the effect of stratification and internal waves. *Nonlinear Processes Geophys.*, **22**, 337–348, doi:10.5194/npg-22-337-2015.

Ezhova, E. V., and Y. I. Troitskaya, 2012: Nonsteady dynamics of turbulent axisymmetric jets in a stratified fluid: Part 2. Mechanism of excitation of axisymmetric oscillations in a submerged jet. *Izv. Atmos. Ocean. Phys.*, **48**, 528–537, doi:10.1134/S0001433812050027.

——, D. A. Sergeev, A. A. Kandaurov, and Y. I. Troitskaya, 2012: Nonsteady dynamics of turbulent axisymmetric jets in a stratified fluid: Part 1. Experimental study. *Izv. Atmos. Ocean. Phys.*, **48**, 409–417, doi:10.1134/S0001433812040081.

Fischer, P. F., J. W. Lottes, and S. G. Kerkemeier, 2008: Nek5000. Accessed 30 December 2014. [Available online at http://nek5000.mcs.anl.gov.]

Friedman, P. D., 2006: Oscillations in height of a negatively buoyant jet. *J. Fluids Eng.*, **128**, 880–882, doi:10.1115/1.2201647.

——, V. D. Vadokoot, W. J. Meyer, and S. Carey, 2007: Instability threshold of a negatively buoyant fountain. *Exp. Fluids*, **42**, 751–759, doi:10.1007/s00348-007-0283-5.

Germano, M., U. Piomelli, P. Moin, and W. H. Cabot, 1991: A dynamic subgrid-scale eddy viscosity model. *Phys. Fluids*, **3A**, 1760–1765, doi:10.1063/1.857955.

Hunt, J. C. R., 1994: Atmospheric jets and plumes. *Recent Research Advances in the Fluid Mechanics of Turbulent Jets and Plumes*, P. A. Davies and M. J. Valente Neves, Eds., Kluwer Academic Publishers, 309–334.

Hussein, J., S. P. Capp, and W. K. George, 1994: Velocity measurements in a high-Reynolds-number, momentum-conserving, axisymmetric, turbulent jet. *J. Fluid Mech.*, **258**, 31–75, doi:10.1017/S002211209400323X.

Jirka, G. H., and J. H. W. Lee, 1994: Waste disposal in the ocean. *Water Quality and Its Control*, M. Hino, Ed., Balkema, 193–242.

Kamenkovich, V. M., and A. S. Monin, 1978: *Ocean Physics*. Vol. 2. Nauka Publishing House, 439 pp.

Kaye, N. B., and G. R. Hunt, 2006: Weak fountains. *J. Fluid Mech.*, **558**, 319–328, doi:10.1017/S0022112006000383.

Knauss, J., 2005: *Introduction to Physical Oceanography*. 2nd ed. Waveland Press, 320 pp.

Lin, W., and S. W. Armfield, 2000: Direct simulation of weak axisymmetric fountains in a homogeneous fluid. *J. Fluid Mech.*, **403**, 67–88, doi:10.1017/S0022112099006953.

Lin, Y. J. P., and P. F. Linden, 2005: The entrainment due to a turbulent fountain at a density interface. *J. Fluid Mech.*, **542**, 25–52, doi:10.1017/S002211200500635X.

List, E. J., 1982: Turbulent jets and plumes. *Annu. Rev. Fluid Mech.*, **14**, 189–212, doi:10.1146/annurev.fl.14.010182.001201.

Matusov, P. A., L. A. Ostrovsky, and L. S. Tsimring, 1989: Amplification of small scale turbulence by the internal waves. *Dokl. Acad. Sci. USSR*, **307**, 979–984.

McDougall, T. J., 1981: Negatively buoyant vertical jets. *Tellus*, **33A**, 313–320, doi:10.1111/j.2153-3490.1981.tb01754.x.

Morton, B. R., G. Taylor, and J. S. Turner, 1956: Turbulent gravitational convection from maintained and instantaneous sources. *Proc. Roy. Soc. London*, **A234**, 1–25, doi:10.1098/rspa.1956.0011.

Ohlsson, J., P. Schlatter, P. F. Fischer, and D. S. Henningson, 2010: Large eddy simulation of turbulent flow in a plane asymmetric diffuser by the spectral-element method. *Direct and Large-Eddy Simulation VII*, V. Armenio, B. Geurts, and J. Fröhlich, Eds., ERCOFTAC Series, Vol. 13, Springer, 197–204, doi:10.1007/978-90-481-3652-0_29.

Orlanski, I., 1976: A simple boundary condition for unbounded hyperbolic flows. *J. Comput. Phys.*, **21**, 251–269, doi:10.1016/0021-9991(76)90023-1.

Panchapakesan, N. R., and J. L. Lumley, 1993: Turbulence measurements in axisymmetric jets of air and helium. Part 1. Air jet. *J. Fluid Mech.*, **246**, 197–223, doi:10.1017/S0022112093000096.

Pham, M. V., F. Plourde, S. K. Doan, and S. Balachandar, 2006: Large-eddy simulation of a pure thermal plume under rotating conditions. *Phys. Fluids*, **18**, 015101, doi:10.1063/1.2162186.

——, ——, and ——, 2007: Direct and large-eddy simulations of a pure thermal plume. *Phys. Fluids*, **19**, 125103, doi:10.1063/1.2813043.

Picano, F., and C. S. Casciola, 2007: Small-scale isotropy and universality of axisymmetric jets. *Phys. Fluids*, **19**, 118106, doi:10.1063/1.2804955.

——, and K. Hanjalic, 2012: Leray-α regularization of the Smagorinsky-closed filtered equations for turbulent jets at high Reynolds numbers. *Flow Turbul. Combust.*, **89**, 627–650, doi:10.1007/s10494-012-9413-0.

Pope, S., 2000: *Turbulent Flows.* Cambridge University Press, 802 pp.

Sciascia, R., F. Straneo, C. Cenedese, and P. Heimbach, 2013: Seasonal variability of submarine melt rate and circulation in an east Greenland fjord. *J. Geophys. Res. Oceans*, **118**, 2492–2506, doi:10.1002/jgrc.20142.

Shrinivas, A. B., and G. R. Hunt, 2014: Unconfined turbulent entrainment across density interfaces. *J. Fluid Mech.*, **757**, 573–598, doi:10.1017/jfm.2014.474.

——, and ——, 2015: Confined turbulent entrainment across density interfaces. *J. Fluid Mech.*, **779**, 116–143, doi:10.1017/jfm.2015.366.

Shy, S. S., 1995: Mixing dynamics of jet interaction with a sharp density interface. *Exp. Therm. Fluid Sci.*, **10**, 355–369, doi:10.1016/0894-1777(94)00095-P.

Smagorinsky, J., 1963: General circulation experiments with the primitive equations. *Mon. Wea. Rev.*, **91**, 99–164, doi:10.1175/1520-0493(1963)091<0099:GCEWTP>2.3.CO;2.

Stewart, R. H., 2008: *Introduction to Physical Oceanography.* Texas A&M University, 345 pp.

Straneo, F., and C. Cenedese, 2015: Dynamics of Greenlands glacial fjords and their role in climate. *Annu. Rev. Mar. Sci.*, **7**, 89–112, doi:10.1146/annurev-marine-010213-135133.

——, R. Curry, D. Sutherland, G. Hamilton, C. Cenedese, K. Vage, and L. Stearns, 2011: Impact of fjord dynamics and glacial runoff on the circulation near Helheim Glacier. *Nat. Geophys.*, **4**, 322–327, doi:10.1038/ngeo1109.

Troitskaya, Y. I., D. A. Sergeev, E. V. Ezhova, I. A. Soustova, and V. I. Kazakov, 2008: Self-induced internal waves excited by buoyant plumes in a stratified tank. *Dokl. Earth Sci.*, **419**, 506–510, doi:10.1134/S1028334X08030343.

Turner, J. S., 1966: Jets and plumes with negative or reversing buoyancy. *J. Fluid Mech.*, **26**, 779–792, doi:10.1017/S0022112066001526.

——, 1973: *Buoyancy Effects in Fluids.* Cambridge University Press, 367 pp.

Williamson, N., N. Srinarayana, S. W. Armfield, G. D. McBain, and W. Lin, 2008: Low-Reynolds-number fountain behaviour. *J. Fluid Mech.*, **608**, 297–317, doi:10.1017/S0022112008002310.